– Supporting Information –

Sono-Cavitation and Nebulization-Based Synthesis of Conjugated Microporous Polymers for Energy Storage Applications

Deok-Ho Roh,[§,†] *HyeonOh Shin,*[§,†] *Hyun-Tak Kim,*[§,†,‡] *and Tae-Hyuk Kwon**[,†]

[†]Department of Chemistry and Center for Wave Energy Materials, Ulsan National Institute of Science and Technology (UNIST), Ulsan 44919, Republic of Korea

[‡]Center for Environment & Sustainable Resources, Korea Research Institute of Chemical Technology (KRICT), Daejeon 34114, Republic of Korea

[§]These authors contributed equally to this work

*Corresponding author. Email: kwon90@unist.ac.kr

Table of Contents

1. General information

400 MHz Fourier-transform nuclear magnetic resonance (NMR)

Liquid-state ^{1}H and ^{13}C NMR were carried out using a Bruker Ascend 400 MHz FT-NMR spectrometer at 25 °C. ^{13}C cross-polarization magic angle spinning solid-state NMR (CP-MAS NMR) measurements were performed using an Agilent VNMRS 600 MHz FT-NMR spectrometer at 25 °C. Data analyses were conducted using a MestReNova (MNova) program.

Fourier-transform infrared (FTIR) spectroscopy

FTIR spectra were obtained by using attenuated total reflection (ATR) geometry on a Varian 670/620 FTIR spectrometer under room temperature. FTIR spectra of conjugated microporous polymer (CMP) films were recorded on a quartz glass substrate. On the other hand, FTIR spectra of CMPs produced from a conventional synthetic method and monomers were measured as powdered samples.

Two-dimensional (2D) grazing incidence wide angle X-ray diffraction (GIWAXD)

2D GIWAXD measurements were performed at the PLS-II 6D UNIST-PAL beamline of the Pohang Accelerator Laboratory in Korea. The X-ray coming from the bending magnet was monochromated (l = 1.06 Å) using a double-crystal monochromator (DCM) and focused using a sagittal focusing DCM and bendable toroidal mirror system (beam size: 150 mm (H) × 120 mm (V) in full width at half maximum (FWHM) at sample position). The 2D GIWAXD measurement system was equipped with a six-axis motorized sample stage inside a vacuum chamber (~2×10^{-2} Torr) to enable the fine alignment of a thin-film sample and effective removal of unwanted air and window scattering. The 2D GIWAXD patterns were recorded using a 2D CCD detector (Rayonix MX225-HS, USA), and the diffraction angles were calibrated using a pre-calibrated sucrose sample (monoclinic, P21, a = 10.9127 Å, b = 8.6812 Å, c = 7.691 Å, and b = 103.109°).

N_2 sorption isotherms measurement and porosity characterization

N_2 sorption isotherms were performed at 77 K with Physisorption Analyzer (ASAP2420, Micromeritics Instruments) after degassing the samples under high vacuum at 150 °C for 5 h. Note that the measurements were conducted on powder-form CMP-BT (120 and 180 kHz) obtained from the film-state CMP-BT. The Brunauer–Emmett–Teller (BET), t-plot, and Horvath–Kawazoe models were used to calculate the specific surface areas, micropore areas and median micropore

width of the CMP samples, respectively. The different relative pressure ranges of adsorption branches were applied to each method (BET: 0.01–0.1 P/P_0, t-plot: total region, Horvath–Kawazoe: up to 0.01 P/P_0). The non-local density functional theory (NLDFT) method was used to estimate the pore size distribution.

Scanning electron microscopy (SEM)

SEM measurements were performed using a FEI Nobs NanoSEM 230 instrument operating at an accelerating voltage of 10.0 kV.

High resolution-transmission electron microscopy (HR-TEM)

HR-TEM images of CMP-BT (180 kHz) and CMP-BT/CNT-1:1 were obtained using a JEOL JEM-2100F instrument operating at an accelerating voltage of 200 kV. Sample preparation of CMP-BT (180 kHz) for HR-TEM measurements was as follows. CMP films were detached from indium tin oxide (ITO) glasses by sonication. The detached films were dispersed in THF solvent through sonication and magnetic stirring. The CMP dispersions were deposited on 400-mesh Cu grids by drop casting technique. Afterward, the samples were dried in an oven at 75 °C overnight. Sample preparation of CMP-BT/CNT-1:1 for the measurements is described in the text below.

Focus ion beam (FIB)

Cross-sectional sample of CMP-BT/CNT-1:1 for SEM and HR-TEM measurements was prepared by using a FEI Helios NanoLab 450 (FIB) instrument operating at an accelerating voltage 3.0 kV.

X-ray photoelectron spectroscopy (XPS)

XPS and elemental composition analysis of CMP films were carried out using a ThermoFisher K-alpha.

UV–vis–NIR absorption spectroscopy

UV–vis spectra were obtained using a SHIMADZU UV-2600 spectrometer. Monomers (1 wt % in chloroform) were fabricated on quartz glasses by spin-coating method. CMP films were fabricated on quartz glasses using 10 cycles of SNS. UV–Vis–NIR spectra of neutral and oxidized CMP films were recorded using an Agilent Cary 5000 instrument. CMP films were fabricated on ITO glasses using 10 cycles of SNS. CMP films on ITO glasses were oxidized at 1.4 V in a three-electrode system until fully oxidized. The oxidized CMP films were washed with acetonitrile to remove residual compounds and dried before UV–vis–NIR measurement.

Specific capacitances calculations

The capacitance of electrodes were calculated using the voltammetric discharge integrated from cyclic voltammetry (CV) curves over the potential range according to the following equation:

$$C\ (\mathrm{F}) = \frac{1}{2}\int_{V_{\mathrm{initial}}}^{V_{\mathrm{final}}} IdV \cdot \frac{1}{(V_{\mathrm{final}} - V_{\mathrm{initial}})v} \qquad \text{eq (S1)}$$

where V_{initial} (V) and V_{final} (V) are the starting and end potential in the CV curves, I (A) is the instantaneous current at a given potential, and v (V/s) is the scan rate, respectively.

The discharge capacitances were calculated from galvanostatic charge-discharge (GCD) curves according to the following equation:

$$C\ (\mathrm{F}) = \frac{I \cdot \Delta t}{(V_{\mathrm{final}} - V_{\mathrm{initial}})} \qquad \text{eq (S2)}$$

where I (A) is the discharge current, Δt (s) is the discharge time consumed from V_{initial} to V_{final}, and $(V_{\mathrm{initial}} - V_{\mathrm{final}})$ is the potential window, respectively.

The gravimetric capacitance and the areal capacitance of the electrodes were calculated according to the following equations:

$$C_{\mathrm{Gravimetric}}\ (\mathrm{F/g}) = C\ (\mathrm{F})/m\ (\mathrm{g}) \qquad \text{eq (S3)}$$

$$C_{\mathrm{Areal}}\ (\mathrm{F/cm^2}) = C\ (\mathrm{F})/A\ (\mathrm{cm^2}) \qquad \text{eq (S4)}$$

where m (g) and A ($\mathrm{cm^2}$) are the mass and geometric surface area of the electrode, respectively.

Energy and power densities calculations

The energy density was calculated according to the following equation:

$$E\ (\mathrm{Wh/kg}) = \frac{1}{2} C_{\mathrm{sp}} (\Delta V)^2 \times \frac{1}{3.6} \qquad \text{eq (S5)}$$

where E (Wh/kg) is the energy density, C_{sp} (F/g) is the specific capacitance, ΔV (V) is the potential window of discharge, and the (1/3.6) is the constant for converting sec to hour and gram (g) to kilogram (kg) unit.

The power density was calculated according to the following equation:

$$P\ (\mathrm{W/kg}) = \frac{E\ (\mathrm{Wh/kg})}{\Delta t} \times 3600 \qquad \text{eq (S6)}$$

where P (W/kg) is the power density, E (Wh/kg) is the energy density, Δt (sec) is the discharging time, and the 3600 is the constant for converting sec to hour.

2. Synthetic procedures

The syntheses of intermediated compounds **1**, **2**, **4**, **6**, **M-TPA, M-DTT**, and **M-BT** were carried out based on previous literature procedures.[1–3]

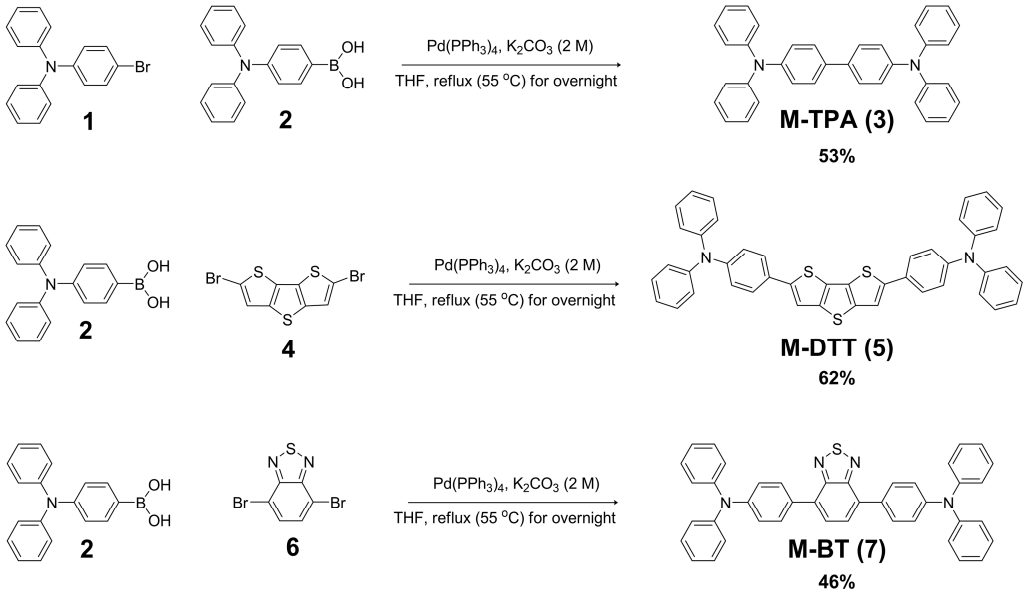

Figure S1. Synthesis scheme of the monomers.

***N*⁴,*N*⁴,*N*⁴',*N*⁴'-tetraphenylbiphenyl-4,4'-diamine (M-TPA, 3)**

Compound **1** (800 mg, 2.47 mmol), compound **2** (780 mg, 2.70 mmol), and $Pd(PPh_3)_4$ (86 mg, 74.4 μmol) were added to a 100 mL two-neck round-bottom flask with a magnetic stirrer bar, and the flask was evacuated under vacuum for 30 min. Afterward, 50 mL of degassed THF and 5.0 mL of degassed 2 M K_2CO_3 (aq) were injected into the flask, followed by flusing with Ar gas. The reaction solution was stirred overnight at 55 °C under Ar atmosphere. When the reaction had completed, H_2O (15 mL) was added to quench the reaction. The resulting mixture was diluted with CH_2Cl_2 (100 mL) and washed with H_2O (3 × 100 mL). The organic layer was collected, dried over anhydrous $MgSO_4$, and evaporated under reduced pressure. The crude product was purified by column chromatography using hexane/CH_2Cl_2 mixture (*v*/*v* = 4:1) as eluent to give compound **3** (640 mg, 1.31 mmol, 53%) as white solid. ^{1}H NMR (400 MHz, $CDCl_3$) δ (ppm): 7.44–7.45 (d, *J* = 7.2 Hz, 4H), 7.24−7.28 (t, *J* = 7.0 Hz 8H), 7.11–7.13 (d, *J* = 7.2 Hz, 12H), 7.00–7.04 (t, *J* = 6.8 Hz, 4H). ^{13}C NMR (100 MHz, $CDCl_3$) δ (ppm): 147.71, 146.72, 134.69, 129.23, 127.28, 124.29, 124.06, 122.80. FTIR (ATR) υ (cm^{-1}): 3086 (w), 3059 (w), 3032 (w), 2960 (w), 2927 (w), 1587 (m), 1487 (s), 1329 (m), 1323 (m), 1277 (s), 1174 (w), 1155 (w), 1076 (w), 1026 (w), 1003 (w), 923 (w), 897 (w), 849 (w), 820 (m), 752 (s), 737 (m), 717 (w), 698 (s).

4,4'-(dithieno[3,2-b;2′,3′-d]thiophene-2,5-diyl)bis(*N*,*N*-diphenylaniline) (M-DTT, 5)

Compound **4** (685 mg, 1.93 mmol), compound **2** (1.23 g, 4.25 mmol), and $Pd(PPh_3)_4$ (67 mg, 58.0 μmol) were added to a 100 mL two-neck round-bottom flask with a magnetic stirrer bar, and the flask was evacuated under vacuum for 30 min. Afterward, 50 mL of degassed THF and 15 mL of degassed 2 M K_2CO_3 (aq) were injected into the flask, followed by flusing with Ar gas. The reaction solution was stirred overnight at 55 °C under Ar atmosphere. When the reaction had completed, H_2O (15 mL) was added to quench the reaction. The resulting mixture was diluted with CH_2Cl_2 (100 mL) and washed with H_2O (3 × 100 mL). The organic layer was collected, dried over anhydrous $MgSO_4$, and evaporated under reduced pressure. The crude product was purified by column chromatography using hexane/CH_2Cl_2 mixture (*v*/*v* = 4:1) as eluent to give compound **5** (819 mg, 1.20 mmol, 62%) as yellow solid. ^{1}H NMR (400 MHz, DMSO-d_6) δ (ppm): 7.85 (s, 2H), 7.61–7.63 (d, *J* = 6.8 Hz, 4H), 7.33–7.37 (t, *J* = 6.8 Hz, 8H), 7.07–7.12 (m, 12H), 7.00-7.02 (d, *J* = 6.8 Hz, 4H). ^{13}C NMR (100 MHz, DMSO-d_6) δ (ppm): 146.74, 144.12, 141.70, 129.70, 128.53, 127.58, 127.33, 126.40, 124.45, 123.60, 122.91. FTIR (ATR) υ (cm^{-1}): 3083 (w), 3059 (w), 3030 (w), 2956 (w), 2922 (w), 1736 (w), 1587 (s), 1522 (m), 1483 (s), 1329 (m), 1315 (m), 1273 (s), 1192 (w), 1173 (w), 1153 (w), 1111 (w), 1076 (w), 1026 (w), 962 (w), 918 (w), 893 (w), 835 (m), 806 (m), 750 (s), 725 (m), 692 (s).

4,4'-(benzo[*c*][1,2,5]thiadiazole-4,7-diyl)bis(*N*,*N*-diphenylaniline) (M-BT, 7)

Compound **6** (2.00 g, 6.80 mmol), compound **2** (4.71 g, 16.3 mmol), and $Pd(PPh_3)_4$ (236 mg, 204 μmol) were added to a 100 mL two-neck round-bottom flask with a magnetic stirrer bar, and the flask was evacuated under vacuum for 30 min. Afterward, 50 mL of degassed THF and 13.6 mL of degassed 2 M K_2CO_3 (aq) were injected into the flask, followed by flusing with Ar gas. The reaction solution was stirred overnight at 55 °C under Ar atmosphere. When the reaction had completed, H_2O (15 mL) was added to quench the reaction. The resulting mixture was diluted with CH_2Cl_2 (200 mL) and washed with H_2O (3 × 200 mL). The organic layer was collected, dried over anhydrous $MgSO_4$, and evaporated under reduced pressure. The crude product was purified by column chromatography using hexane/CH_2Cl_2 mixture (*v*/*v* = 4:1) as eluent to give compound **7** (2.76 g, 4.43 mmol, 65%) as orange solid. ^{1}H NMR (400 MHz, $CDCl_3$) δ (ppm): 7.87–7.90 (d, *J* = 6.8 Hz, 4H), 7.74 (s, 2H), 7.28–7.32 (t, *J* = 6.8 Hz, 8H), 7.19–7.23 (t, *J* = 8.8 Hz, 12H), 7.05–7.09 (t, *J* = 7.2 Hz, 4H). ^{13}C NMR (100 MHz, $CDCl_3$) δ (ppm): 154.14, 147.96, 147.47, 132.15, 130.99, 129.88, 129.34, 127.42, 124.87, 123.27, 122.92. FTIR (ATR) υ (cm^{-1}): 3062 (w), 3034 (w), 2960 (w), 2924 (w), 2850 (w), 1736 (w), 1587 (s), 1514 (s), 1483 (s), 1331 (s), 1315 (s), 1275 (s), 1192 (w), 1178 (m), 1074 (w), 1026 (w), 883 (m), 835 (m), 821 (s), 752 (s), 731 (m), 694 (s).

3. The droplet size in sono-cavitation and nebulization synthesis

The droplet size of atomized mist is dependent on the ultrasonic frequency, viscosity, and surface tension of a precursor solution. The empirical equation of droplet size derived by Lang is described as follows:[4]

$$D_{droplet} = 0.34\left(\frac{8\pi\gamma}{\rho f^2}\right)^{\frac{1}{3}} \quad \text{eq (S7)}$$

where D (m) is mean diameter of droplet, γ (N/m) is surface tension of solution, ρ (kg/m^3) is solution density, and f (Hz) is the ultrasonic frequency. According to the Lang equation, in sono-cavitation and nebulization synthesis (SNS), the higher ultrasonic frequency of 180 kHz would produce smaller droplets than those generated at the lower ultrasonic frequency of 120 kHz.

Table S1. Solvent parameters for evaluating droplet size.

Ultrasonic frequency, f (kHz)	Solvent	Surface tension, γ (mN/m)	Solution density, ρ (kg/m^3)	Mean diameter of droplet, D (μm)
120	Ethanol	22.1	789	12.4
	Chloroform	27.5	1490	10.8
180	Ethanol	22.1	789	9.49
	Chloroform	27.5	1490	8.26

4. X-ray photoelectron spectroscopy of CMP films

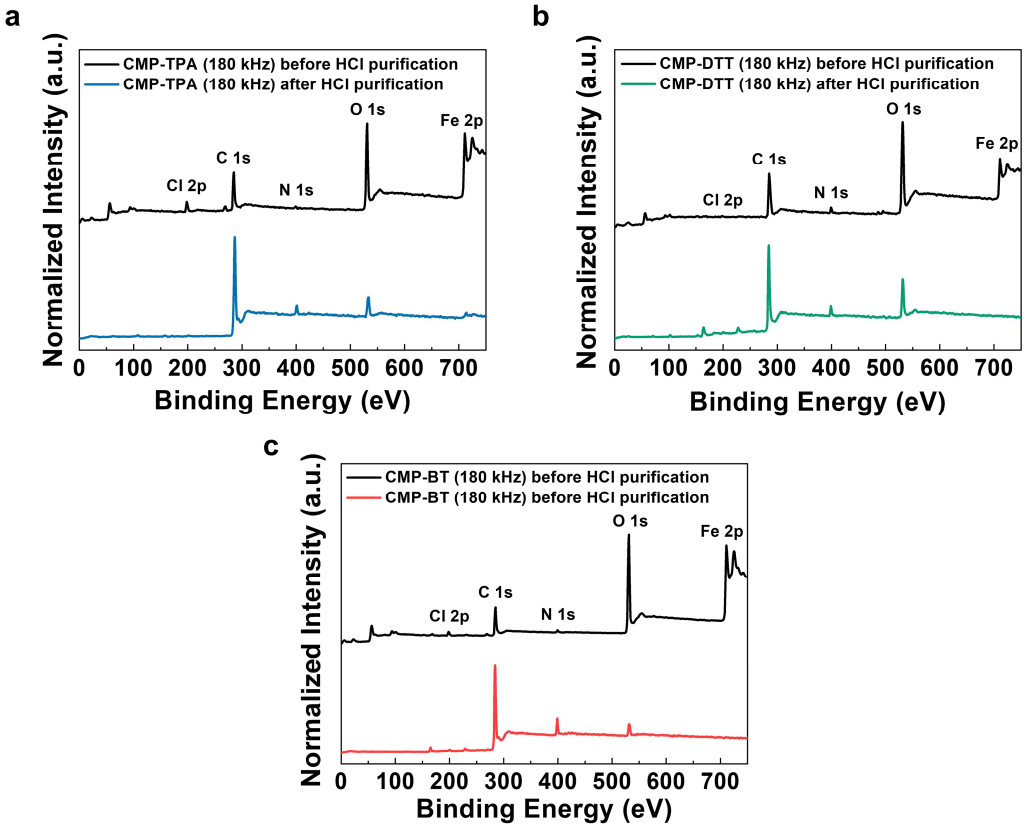

Figure S2. XPS spectra of (**a**) CMP-TPA (180 kHz), (**b**) CMP-DTT (180 kHz), and (**c**) CMP-BT (180 kHz) before (black line) and after (colored line) HCl (0.2 wt %) purification.

Table S2. Atomic composition of CMP (180 kHz) films before and after HCl (0.2 wt %) purification.

Materials	**HCl purification**	**Element (at.%)**					
		C 1s	**N 1s**	**S 2p**	**Fe 2p**	**O 1s**	**Cl 2p**
CMP-TPA (180 kHz)	X	41.58	4.63	0.15	13.36	35.74	4.63
	O	89.49	4.61	0.13	*N/A*	5.26	0.51
Stoichiometry	$C_{36}H_{24}N_2$	94.74	5.26	-	-	-	-
CMP-DTT (180 kHz)	X	39.37	3.18	1.53	6.46	39.37	1.15
	O	73.47	4.91	5.38	*N/A*	13.79	0.79
Stoichiometry	$C_{44}H_{26}N_2S_3$	89.80	4.08	6.12	-	-	-
CMP-BT (180 kHz)	X	35.01	2.14	1.39	12.31	45.69	35.01
	O	83.23	8.35	2.19	0.23	5.33	0.58
Stoichiometry	$C_{42}H_{26}N_4S_1$	89.36	8.51	2.13	-	-	-

5. Large area CMP films of 15 × 15 cm^2 and 25 × 25 cm^2

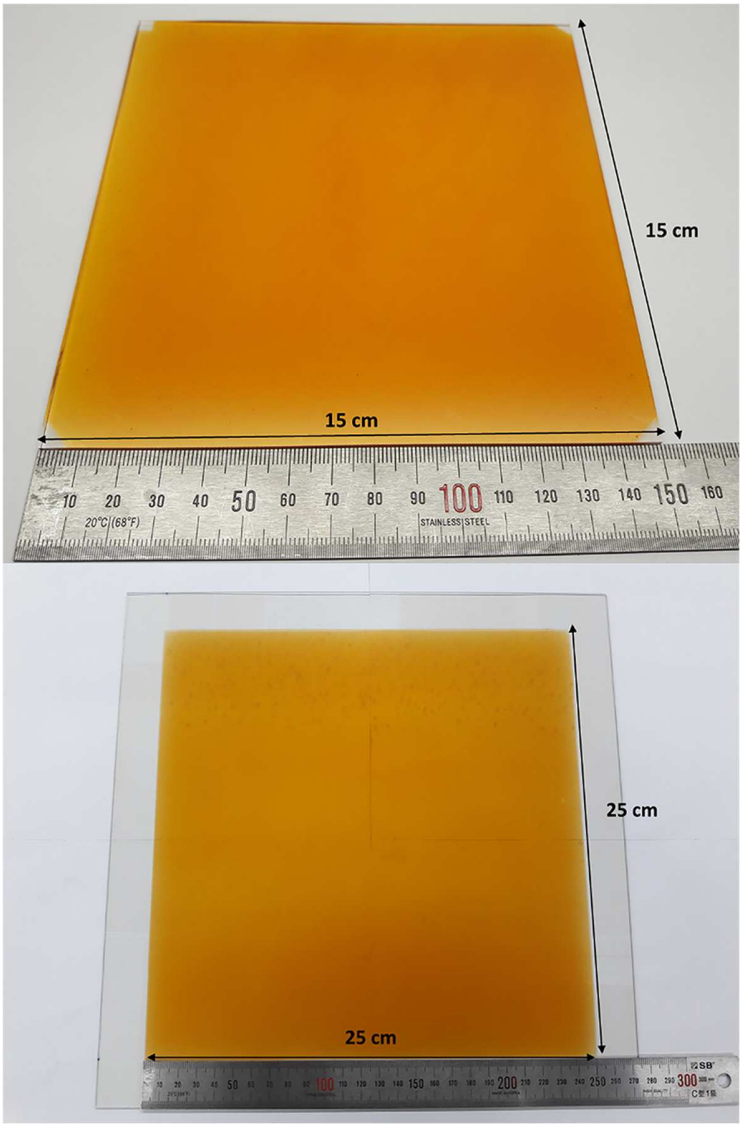

Figure S3. Large area CMP-BT (180 kHz) of 15 × 15 cm^2 and 25 × 25 cm^2. CMP films were fabricated on ITO glass substrates using 10 cycles of SNS.

6. The reaction yield of sono-cavitation and nebulization synthesis

The reaction yield of SNS was calculated as follows.

1. The reaction yield (%) of SNS
   - $\text{Reaction yield (\%)} = \frac{\text{Experimental area mass density for one SNS cycle}}{\text{Theoretical area mass density for one SNS cycle}}$ eq (S8)

2. Parameters of SNS
   - Flow rate (v) = 0.20 mL/min.
   - Mole concentration (C) = 4.0×10^{-4} M.
   - Deposition time (t) = 104.5 min for 25×25 cm^2
   - Molecular weight (M_w) = 488.62 mg/mmol for M-TPA, 682.92 mg/mmol for M-DTT, and 622.78 mg/mmol for M-BT
   - Deposition area (A) = 25×25 cm^2
   - Number of cycles: 1 cycle

3. Evaluating theoretical area mass density for one SNS cycle ($\mu g \cdot cm^{-2} \cdot cycle^{-1}$)
   - Injection volume (mL)
     = v (mL/min) × t (min) eq (S9)
     = 20.9 mL
   - Deposited mass (mg)
     = injection volume (mL) × C (M) × M_w (mg/mmol) eq (S10)
     = $8.36 \times 10^{-3} \cdot M_w$ mg
   - Theoretical area mass density for one SNS cycle ($\mu g \cdot cm^{-2} \cdot cycle^{-1}$)
     = [deposited mass × 10^3 (μg)] / [A (cm^2) × number of cycles] eq (S11)
     = $\frac{8.36}{625} \cdot M_w \ \mu g \cdot cm^{-2} \cdot cycle^{-1}$

Table S3. Theoretical and experimental area mass densities for one SNS cycle.

Materials	Area mass density for one SNS cycle ($\mu g \cdot cm^{-2} \cdot cycle^{-1}$)		
	Theoretical value [a]	120 kHz [b]	180 kHz [b]
CMP-TPA	6.5	3.8 ± 0.2	5.2 ± 0.1
CMP-DTT	9.1	4.6 ± 0.2	6.3 ± 0.2
CMP-BT	8.3	5.3 ± 0.1	6.7 ± 0.1

[a] Theoretical area mass density for one SNS cycle, [b] Experimental area mass density for one SNS cycle. Mean values ± standard deviations are shown, as obtained from four samples.

Table S4. The reaction yields of conventional synthetic method and SNS.

Materials	Yield (%) [a]			
	Conventional synthetic method	120 kHz	180 kHz	180 kHz without thermal energy [b]
CMP-TPA	44 ± 3	57 ± 4	80 ± 2	-
CMP-DTT	50 ± 4	51 ± 2	69 ± 2	-
CMP-BT	81 ± 2	64 ± 1	80 ± 1	67 ± 6

[a] The reaction yields of SNS were calculated using eq (S8) and Table S3. Mean values ± standard deviations are shown, as obtained from four samples. [b] These samples were synthesized at 25 °C (substrate temperature) in the SNS method.

In conventional synthesis of CMPs (a typical polymerization reaction in a round-bottom flask), an electron-donating or electron-withdrawing unit in a monomer structure affects the activity of the oxidative coupling reaction.[5,6] For example, electron-withdrawing units promote radical activity for the para-carbon of TPA, enhancing the activity of the oxidative coupling reaction. Therefore, it is reasonable that M-BT, which possesses an electron-withdrawing unit (benzothiadiazole, BT), showed the highest reaction yield in monomers.

7. Dihydrorhodamine 123 method

The SNS method provides sufficient activation energy for the generation of radical-formed monomers by cavitation process in the ultrasonic nozzle (120 and 180 kHz). To verify the effect of cavitation on SNS, we utilized dihydrorhodamine 123 (DHR123), which is oxidized to the strongly fluorescent rhodamine 123 (R123) by radical species (Figure S4a). This method can be used to estimate the relative amount of the radical species generated from the cavitation process with respect to the ultrasonic frequency (120 and 180 kHz). For this experiment, we prepared the precursor solution comprising 5.0 μM DHR123, 0.50 μM M-TPA, and 10 μM $FeCl_3$ in chloroform/THF (*v*/*v* = 1:1). It should be noted that chloroform/THF (*v*/*v* = 1:1) was used as the solvent instead of chloroform/ethanol (*v*/*v* = 1:1) because ethanol-derived radicals were also generated under ultrasound irradiation. We chose M-TPA as a monomer for this experiment to avoid overlap with the photoluminescence (PL) spectrum of R123. We spayed the precursor solution at different ultrasonic frequencies (120 and 180 kHz) using a flow rate of 0.30 mL/min at room temperature and collected the resulting mist in a flask immediately to prevent solvent evaporation. In addition, we prepared a control sample prepared without any treatment for comparison. Then, we measured the PL of R123 (excitation = 510 nm) of the resulting solutions. As shown in Figure S4b, SNS (180 kHz) showed the highest PL intensity, followed by SNS (120 kHz) and the control sample. This is because the high ultrasonic frequency (180 kHz) provided more activation energy with a more rapid cavitation process than that at low ultrasonic frequency (120 kHz). This result clearly indicates the effect of cavitation in SNS on the chemical reaction.

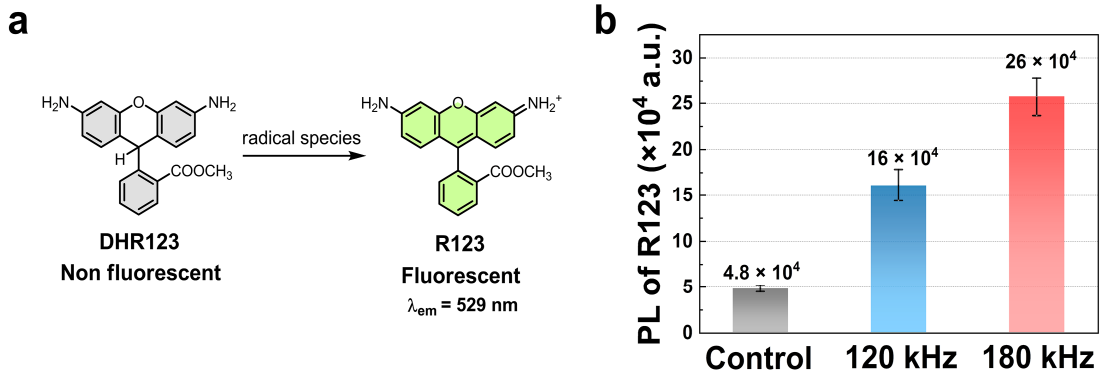

Figure S4. (**a**) Reaction scheme for fluorescent R123 from non-fluorescent DHR123 by radical species. (**b**) PL intensity of R123 after SNS (120 or 180 kHz) treatment of precursor solutions at room temperature. Controls are untreated samples. Precursor solutions consisted of 5.0 μM DHR123, 0.50 μM M-TPA, and 10 μM $FeCl_3$ in chloroform/THF (*v*/*v* = 1:1). The composition of control samples was identical to that of the precursor solution. Denoted values indicate the average values obtained from four samples. Error bars indicate the standard deviation.

8. Spectroscopic characterization of CMP films

We performed ^{13}C cross-polarization magic angle spinning solid-state nuclear magnetic resonance (CP-MAS NMR) analysis to confirm the cross-linked structure of the CMP films prepared using the SNS method. Figure S5a–c show the assignments of the ^{13}C CP-MAS NMR spectra (Figure S5d–h). The peak corresponding to cross-linked carbons was assigned at approximately 135 ppm, as confirmed by comparison M-TPA (8* in Figure S5b). To identify the cross-linked carbon peak clearly, we performed the peak fitting of ^{13}C CP-MAS NMR spectra for the monomers and CMP (180 kHz) using a Gaussian function (Figures 2b and S5g,h). No peak at near 135 ppm was observed in the spectra of the monomers, excluding that for M-TPA of the TPA dimer structure. After polymerization, the cross-linked carbon peak appeared at approximately 135 ppm, as highlighted in red pattern in Figure 2b for CMP-BT, Figure S5g for CMP-TPA, and Figure S5h for CMP-DTT.

Specifically, as shown in Figures 2b and S5d, CMP-BT (120 and 180 kHz) had almost identical ^{13}C CP-MAS NMR spectra to CMP-BT (ref) but exhibited two different peaks compared to M-BT. (i) As shown in Figure 2b, M-BT had a distinct band at approximately 125 ppm, assigned to carbons 1*, 3, and 6 in Figure S5a. After polymerization, the intensity of the peak near 125 ppm decreased in the CMP-BT (120 kHz, 180 kHz, and ref). This is because the para-carbons of TPA units (1* in Figure S5a) react with oxidizing agents ($FeCl_3$), resulting in the cross-linked structure of CMP-BT. Although the carbon atoms (3 and 6 in Figure S5a) are also reactive sites for oxidative coupling because of their electron sufficient property, the significant steric hindrance of the adjacent phenyl ring prevents reaction.[7] (ii) For CMP-BT (120 kHz, 180 kHz, and ref), a new shoulder peak appeared at approximately 135 ppm corresponding to the cross-linked para-carbon of TPA (a* in Figure S5a).

Furthermore, as shown in Figure S5g,h, the spectra of CMP-TPA and CMP-DTT contain peaks corresponding to the cross-linked para-carbon of TPA at approximately 135 ppm and decreased peak intensity at approximately 125 ppm corresponding to 1*, 3, and 6 in M-TPA and M-DTT (Figure S5b,c).

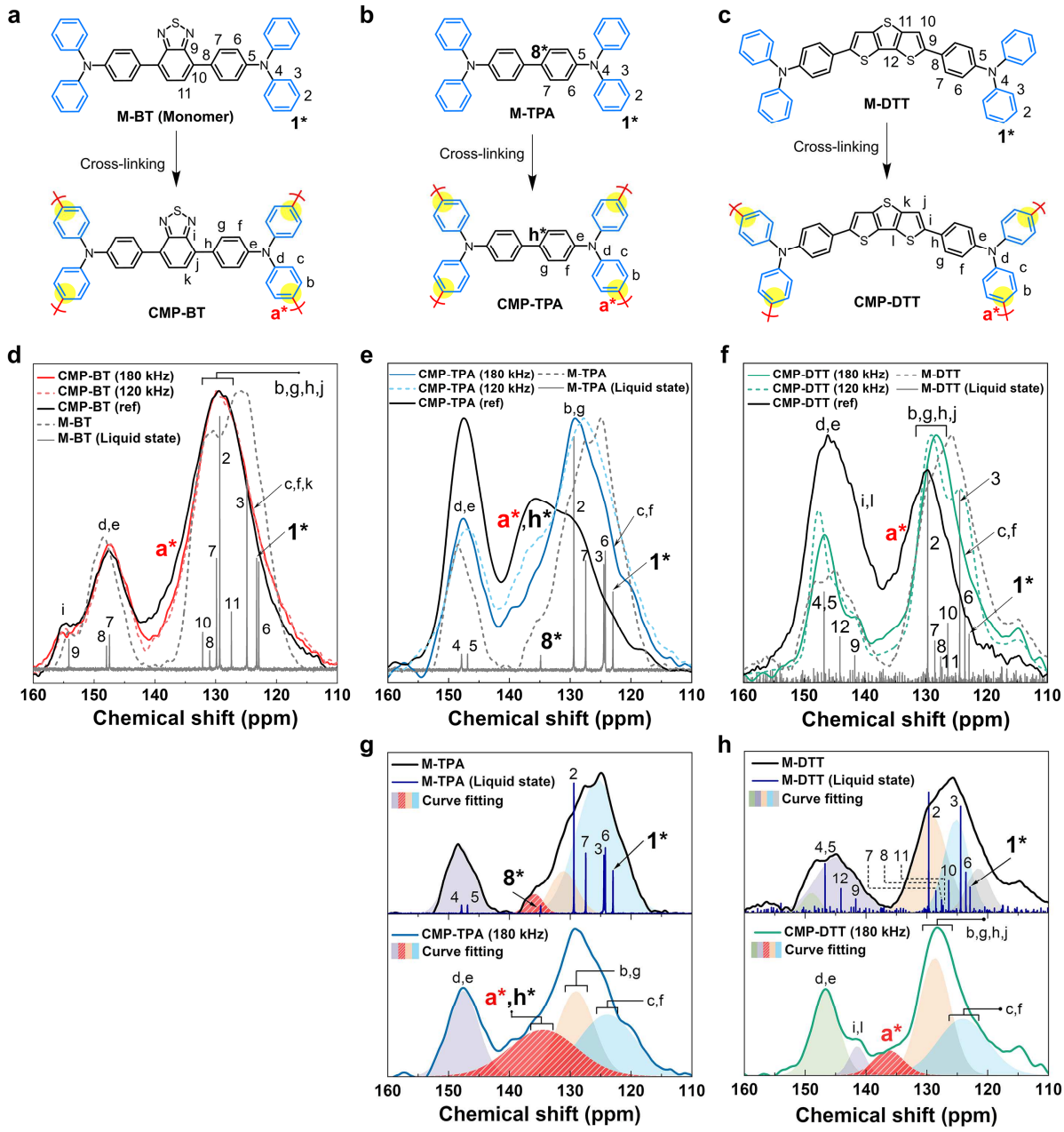

Figure S5. (**a**–**c**) Peak assignments for ^{13}C CP-MAS NMR spectra of monomers and corresponding CMPs. (**d**–**f**) ^{13}C CP-MAS NMR spectra of monomers and CMP (120 and 180 kHz) samples; the liquid-state ^{13}C NMR of monomers measured in a deuterated solvent. (**g** and **h**) Gaussian curve fitting for the ^{13}C CP-MAS NMR spectra of monomers and CMP (180 kHz) samples. The red pattern indicates the peak of the cross-linked para-carbon of TPA.

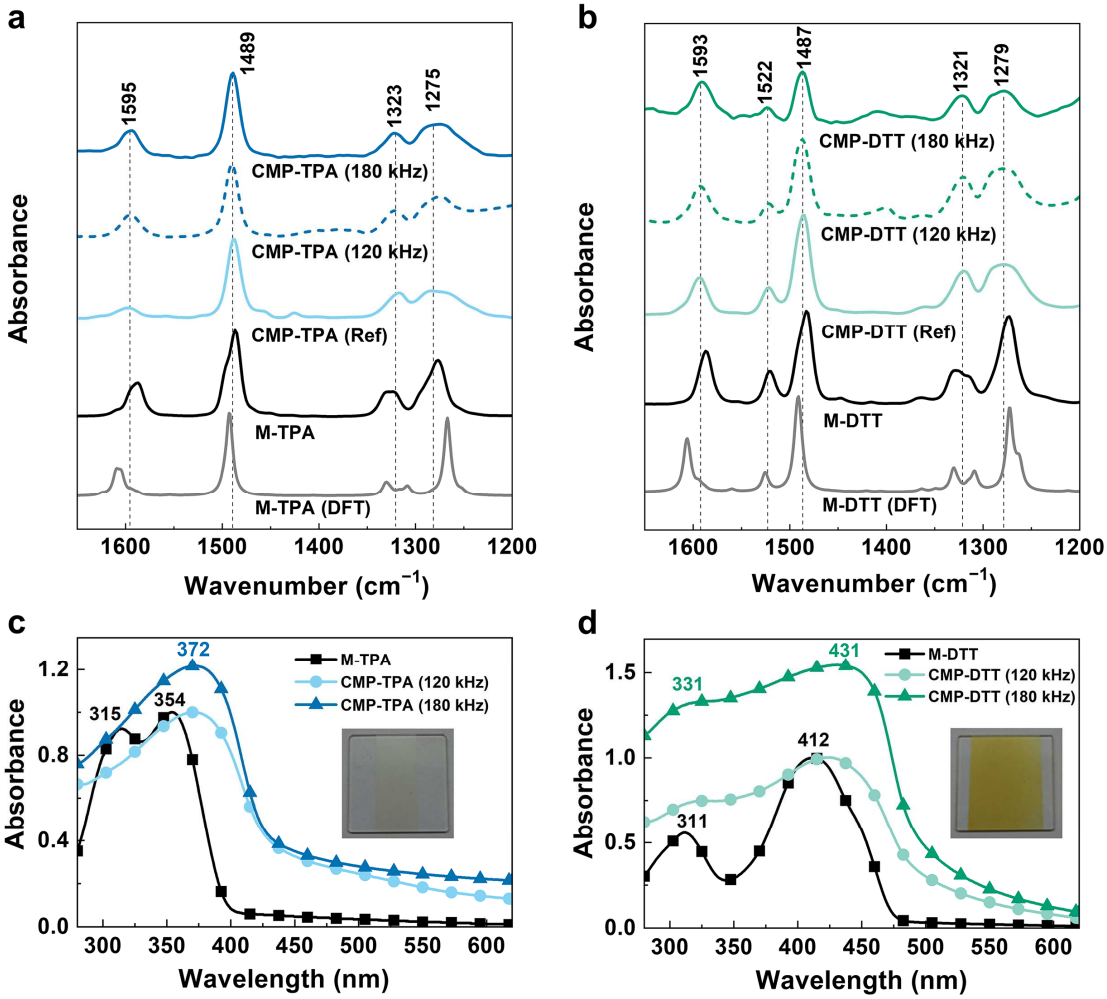

Figure S6. (**a** and **b**) FTIR spectra of monomers, CMP (120 and 180 kHz) films on quartz glasses, and CMPs (ref) along with DFT-calculated IR spectra of the monomers. Wavenumbers of the representative vibration modes of the CMP (180 kHz) films are indicated in the panels. (**c** and **d**) UV–vis spectra of monomers spin-coated on quartz glasses and CMP (120 and 180 kHz) films fabricated on quartz glasses using 10 cycles of SNS. Absorption peaks are indicated in the panels. Inset: photographs of CMP (180 kHz) films on quartz glasses.

9. Density functional theory (DFT) calculations

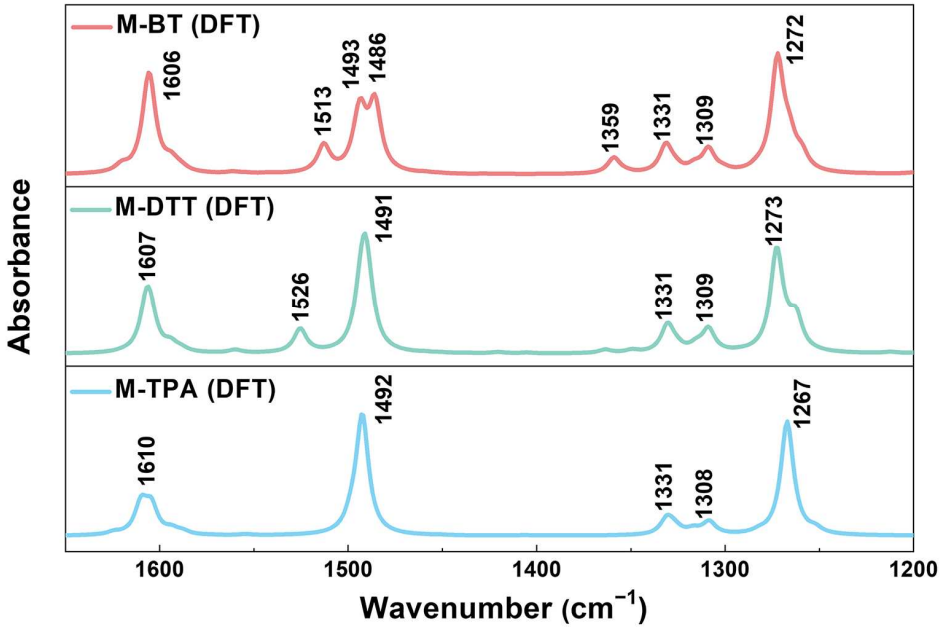

Figure S7. DFT-calculated IR spectra of monomers.

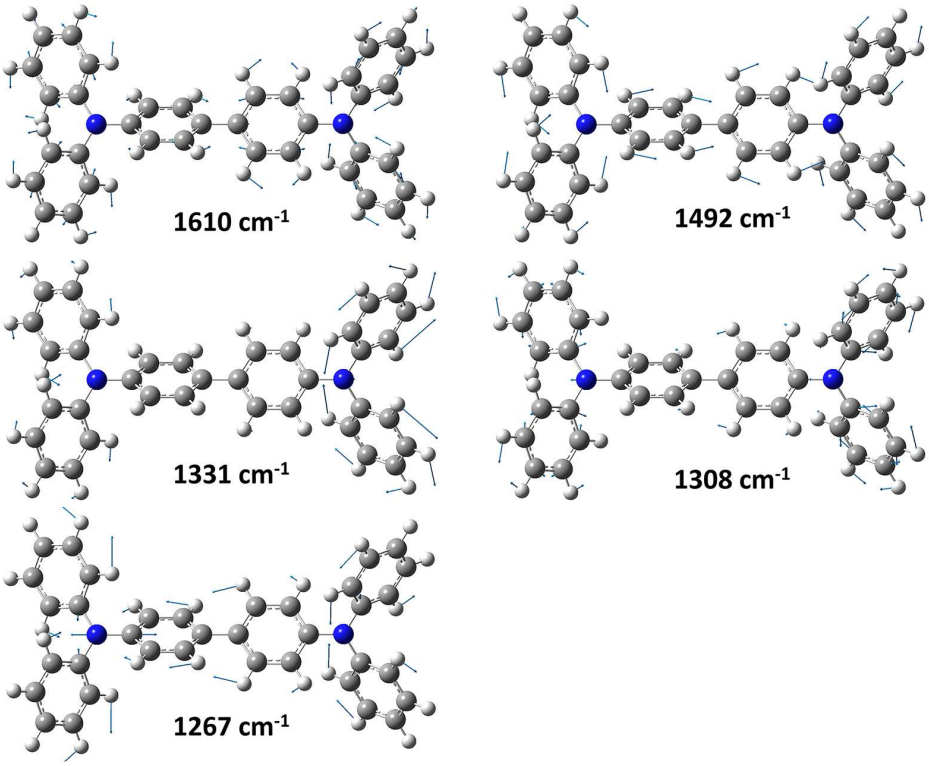

Figure S8. DFT-calculated vibrational modes of M-TPA.

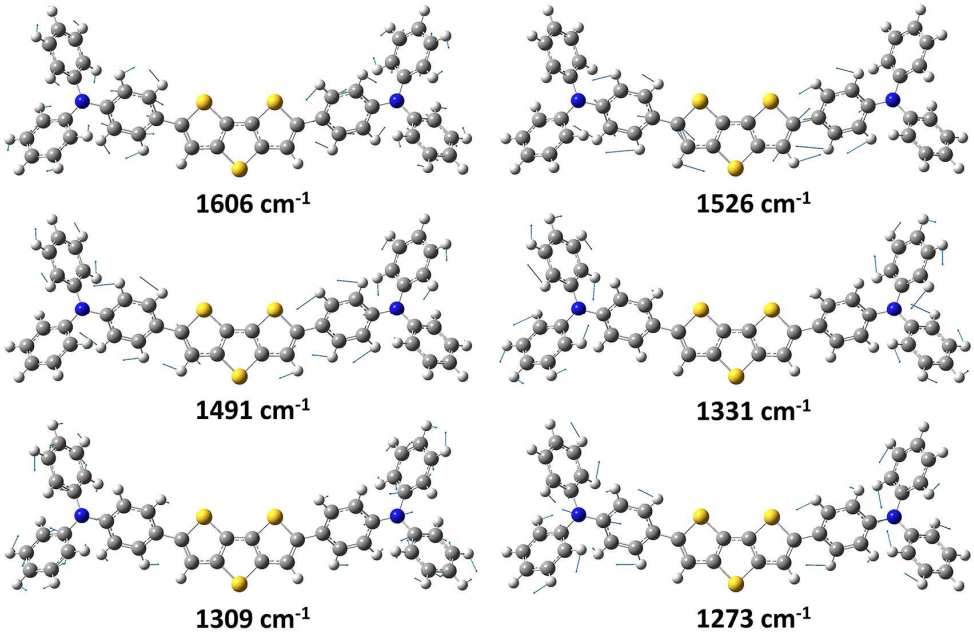

Figure S9. DFT-calculated vibrational modes of M-DTT.

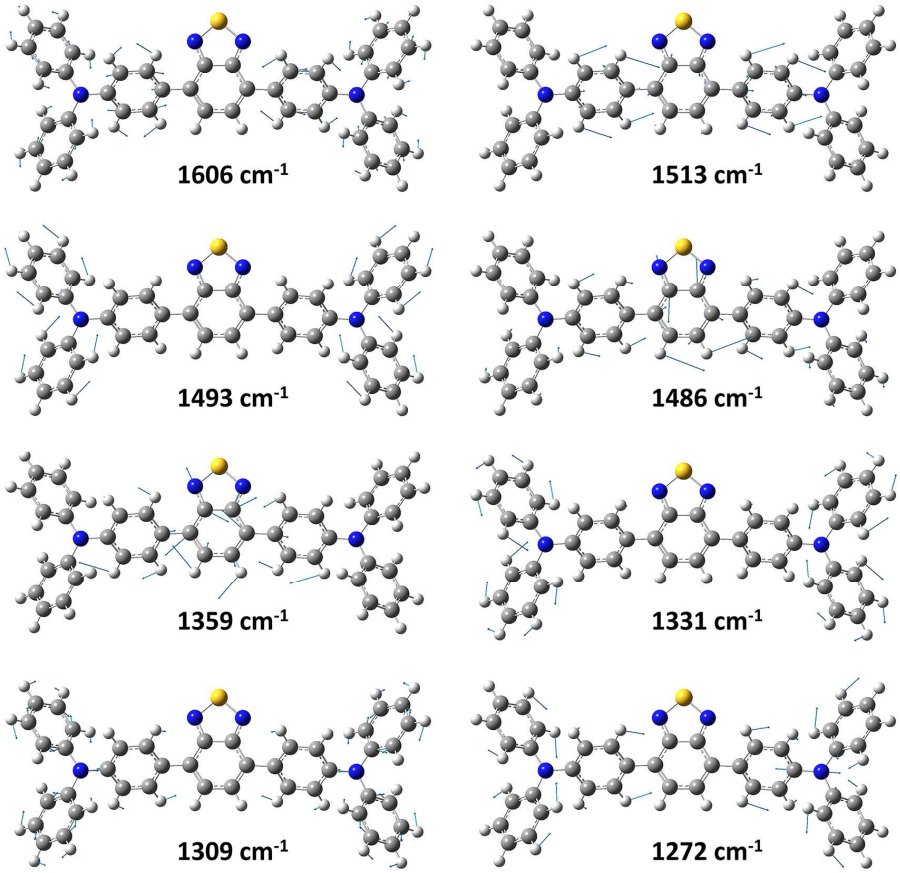

Figure S10. DFT-calculated vibrational modes of M-BT.

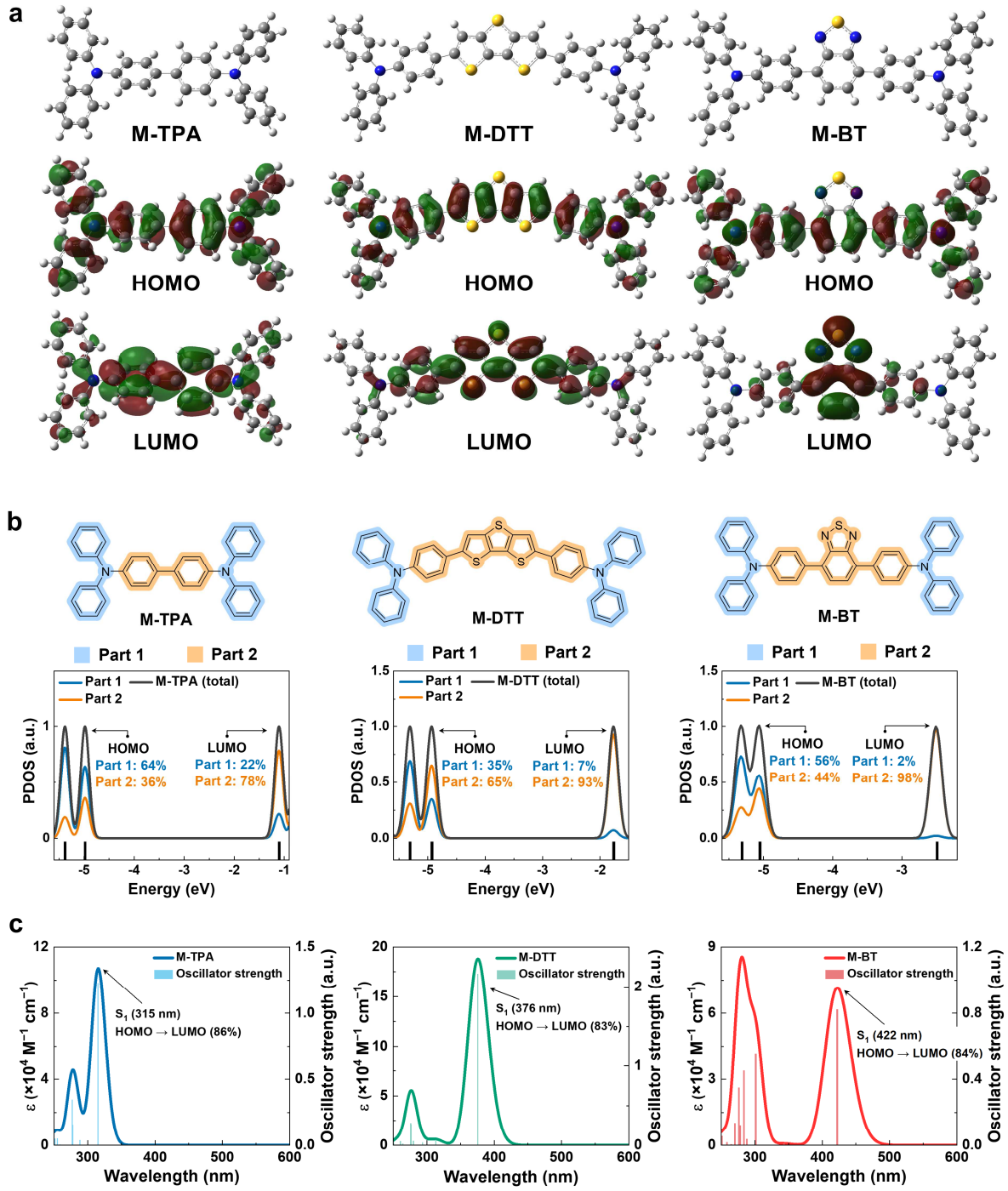

Figure S11. (**a**) Ground-state optimized geometries of monomers and corresponding to the highest occupied molecular orbital (HOMO) and the lowest unoccupied molecular orbital (LUMO). (**b**) Projected density-of-states (PDOS) of the entire monomers and the molecular fragments (part 1 and 2). Percentage contributions of part 1 and 2 to molecular orbital (MO) density in HOMO and LUMO are indicated in each panel. (**c**) Time-dependent DFT calculated UV–vis spectra of the monomers. MOs composition in the electronic transition (S_1) is given in each panel.

10. Grazing incidence wide angle X-ray diffraction (GIWAXD)

We also performed GIWAXD analysis. The feature-rich GIWAXD patterns suggest the formation of a 3D isotropic amorphous film of CMP-BT and the removal of residual compounds after washing with dilute HCl (0.2 wt %). In addition, we confirmed that the higher ultrasonic frequency of 180 kHz in SNS yields CMP films more effectively than the lower ultrasonic frequency of 120 kHz.

As shown in Figures 2e,f and S12a,b, CMP-BT (120 kHz) and CMP-BT (180 kHz) have similar GIWAXD patterns. In CMP-BT (120 kHz), diffuse scattering (q = 0.12–0.48 $Å^{-1}$) and isotropic rings (q = 0.75 and 1.4 $Å^{-1}$) were also observed before and after HCl (0.2 wt %) purification, respectively. However, as shown in Figure S12c,d, CMP-BT (180 kHz) had a higher intensity of isotropic peaks (q = 0.75 and 1.4 $Å^{-1}$) than those of CMP-BT (120 kHz), indicating that the CMP films were effectively synthesized using the high ultrasonic frequency. In addition, before HCl purification, the intensity and shape of the diffuse scattering peak differed based on the ultrasonic frequency of SNS (Figure S12e), indicating that they contained different grain sizes of the unreacted residues and iron compounds.[8] Thus, we evaluated the grain size of the residues using the Scherrer equation:[9–11]

$$\tau = \frac{K\lambda}{\beta \cos \theta} \qquad \text{eq (S12)}$$

where τ is the grain size, K is the Scherrer constant (approximately 0.9), λ is the wavelength of the X-rays (18.986 keV, 15.31 nm), β is the FWHM (Figure S12f), and θ is the Bragg angle (0.12°). CMP-BT (180 kHz) had a smaller grain size (150 nm) than that (310 nm) of CMP-BT (120 kHz). This is because the use of a higher ultrasonic frequency (180 kHz) in SNS consumed more oxidizing agent ($FeCl_3$) and monomer than the use of a lower ultrasonic frequency (120 kHz), resulting in a more aggressive reaction. Thereby, the small amount of unreacted residue in CMP-BT (180 kHz) caused less aggregation with iron compounds than in CMP-BT (120 kHz), resulting in the smaller grain size (150 nm) and confirming the effect of ultrasonic frequency on the reaction in SNS.

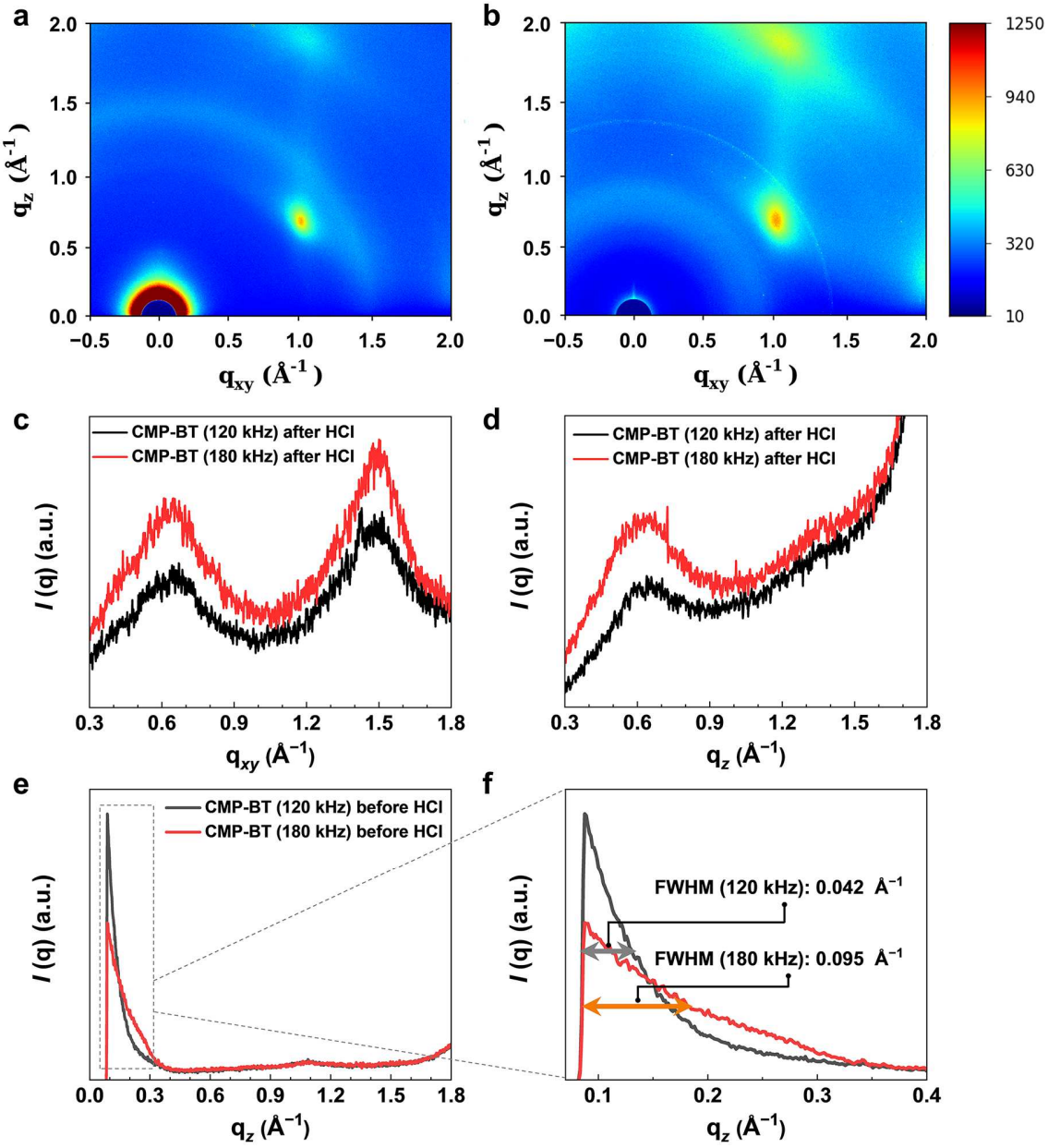

Figure S12. 2D GIWAXD patterns and line-cut profiles of CMP-BT. 2D GIWAXD diffraction patterns of CMP-BT (120 kHz) (**a**) before and (**b**) after HCl (0.2 wt %) purification. (**c**) In-plane and (**d**) out-of-plane line-cut profiles of CMP-BT (120 and 180 kHz) after HCl purification. (**e** and **f**) Out-of-plane line-cut profiles of CMP-BT (120 and 180 kHz) before HCl purification. FWHM of CMP-BT (120 and 180 kHz) are 0.042 Å^{-1} and 0.095 Å^{-1}, respectively. All samples were deposited on Si wafers using 30 cycles of SNS.

11. Free-standing CMP-BT films

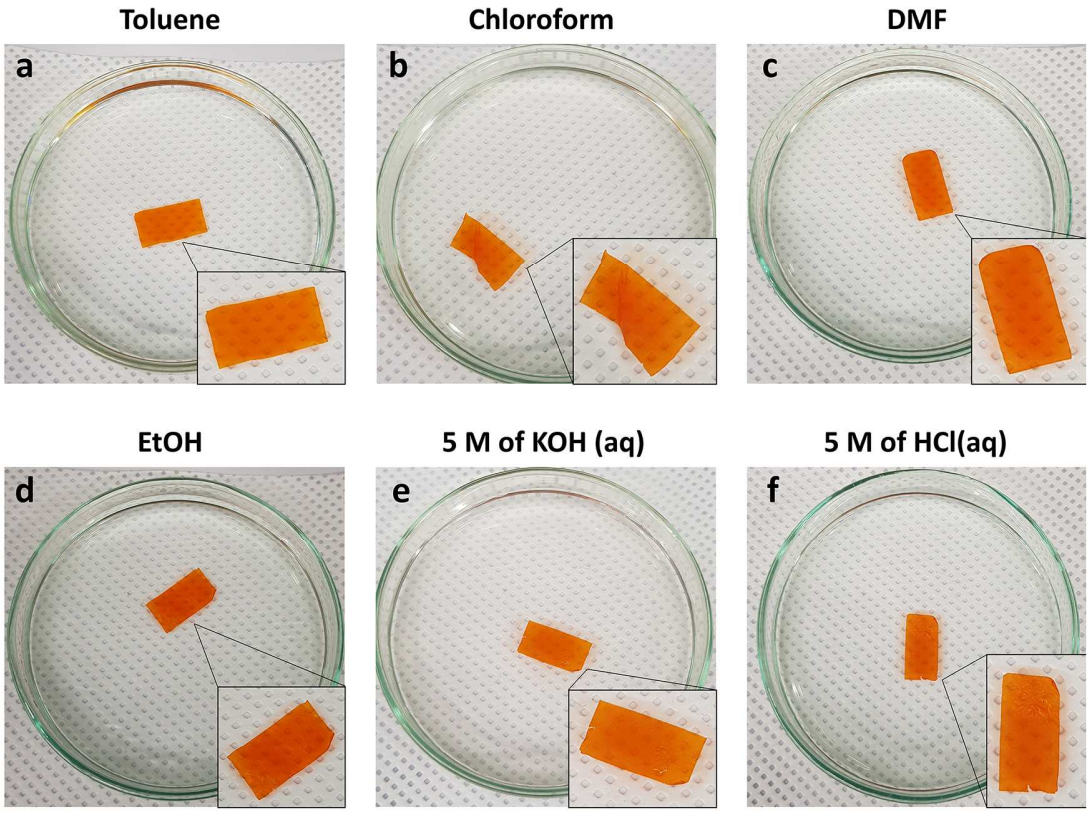

Figure S13. Photographs of free-standing CMP-BT (180 kHz) films in various solvents: (**a**) toluene, (**b**) chloroform, (**c**) DMF, (**d**) ethanol, (**e**) 5 M HCl (aq), and (**f**) 5 M KOH (aq). The free-standing CMP films were prepared as follows: CMP-BT (180 kHz) were synthesized on ITO glass substrates (active area: 1.0 × 2.0 cm^2) using 10 cycles of SNS. The resulting CMP films were soaked in 2 M HCl (aq) for 24 hours. Thereafter, the CMP films can peel off from the ITO glass substrates automatically, becoming free-standing films.

12. Scanning electron microscopy (SEM) images of CMP films

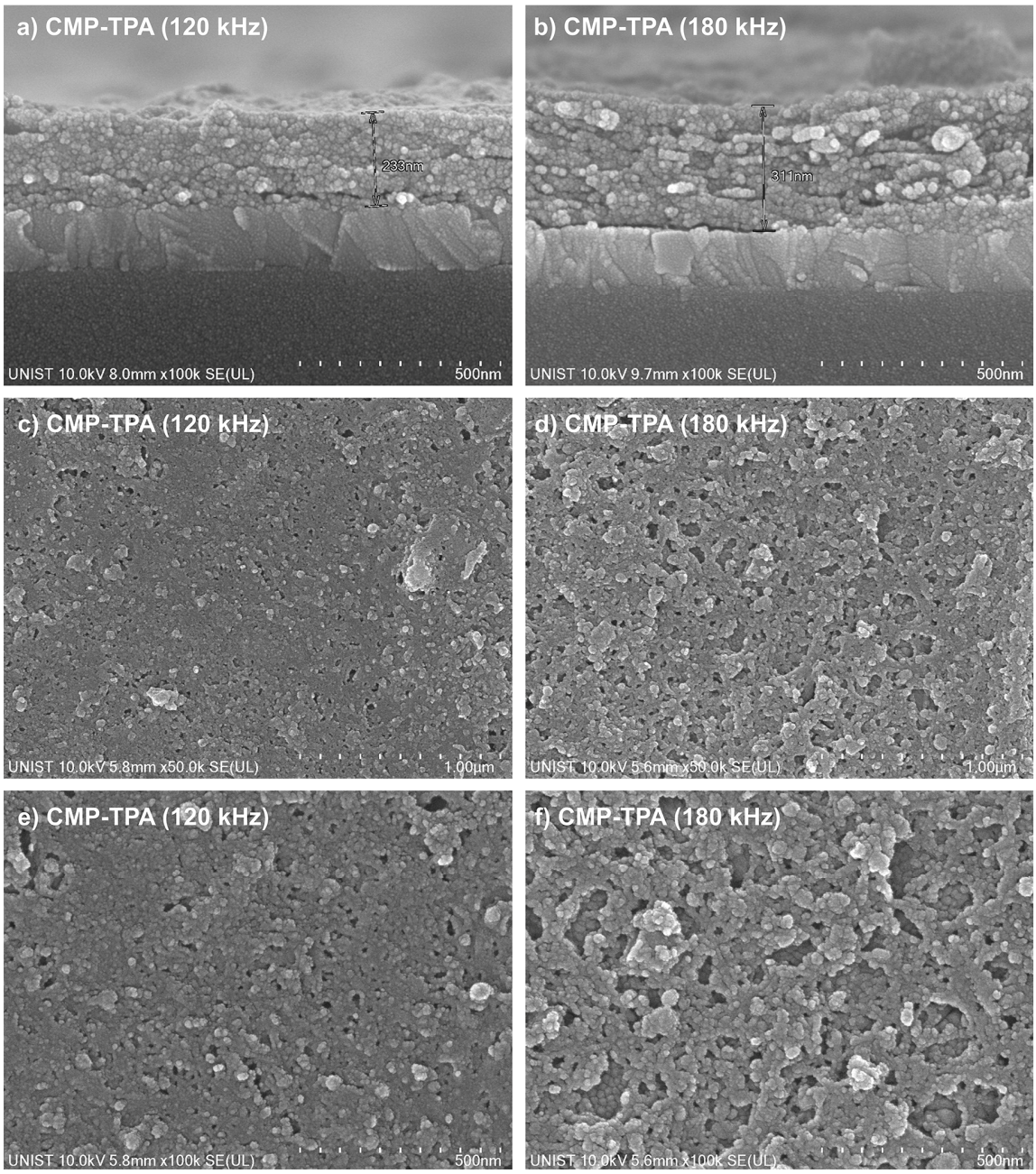

Figure S14. Cross-section SEM images of (**a**) CMP-TPA (120 kHz) and (**b**) CMP-TPA (180 kHz), and surface SEM images of (**c** and **e**) CMP-TPA (120 kHz) and (**d** and **f**) CMP-TPA (180 kHz). CMP-TPA samples were fabricated on ITO glass substrates using 10 cycles of SNS.

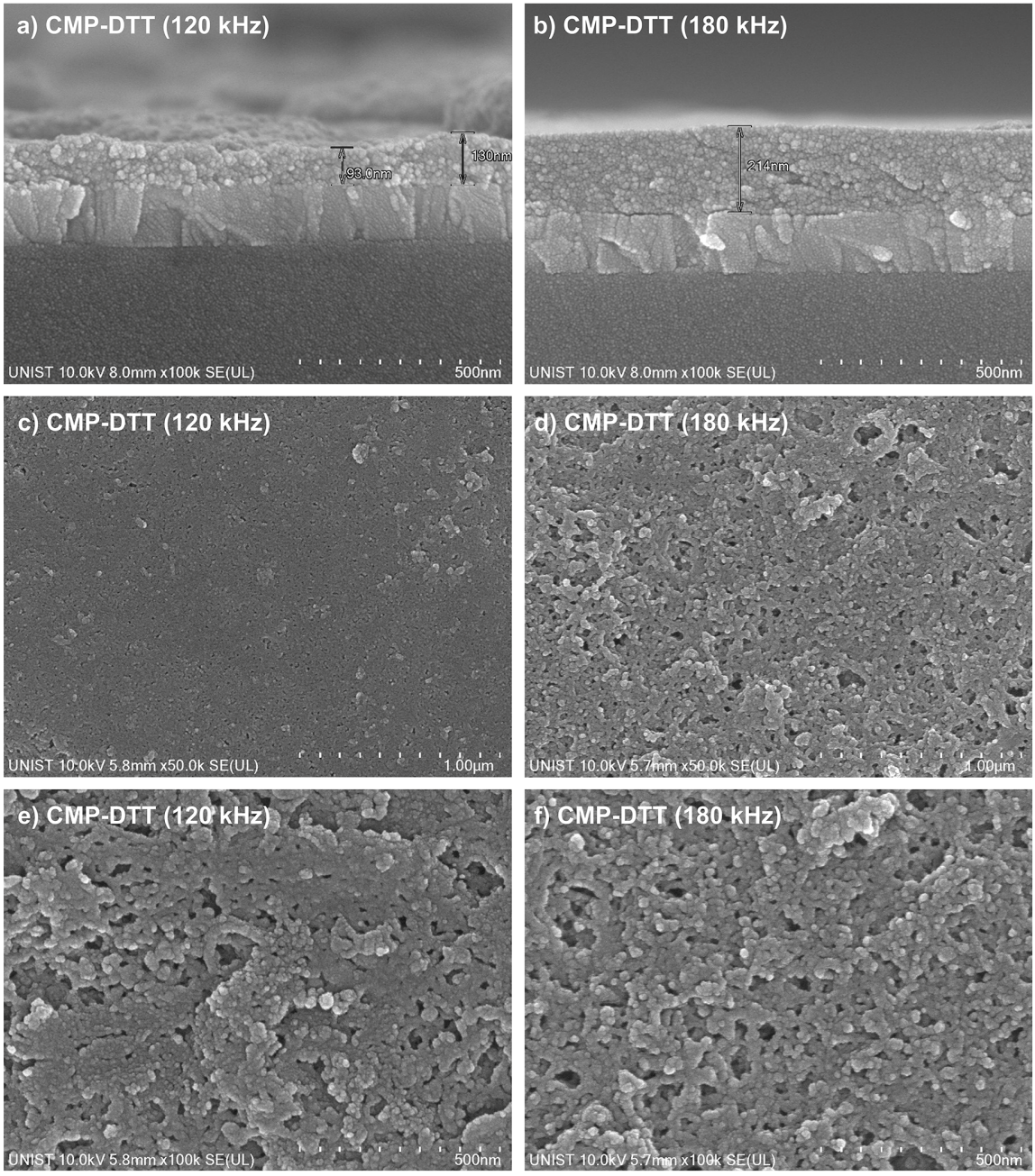

Figure S15. Cross-section SEM images of (**a**) CMP-DTT (120 kHz) and (**b**) CMP-DTT (180 kHz), and surface SEM images of (**c** and **e**) CMP-DTT (120 kHz) and (**d** and **f**) CMP-DTT (180 kHz). CMP-DTT samples were fabricated on ITO glass substrates using 10 cycles of SNS.

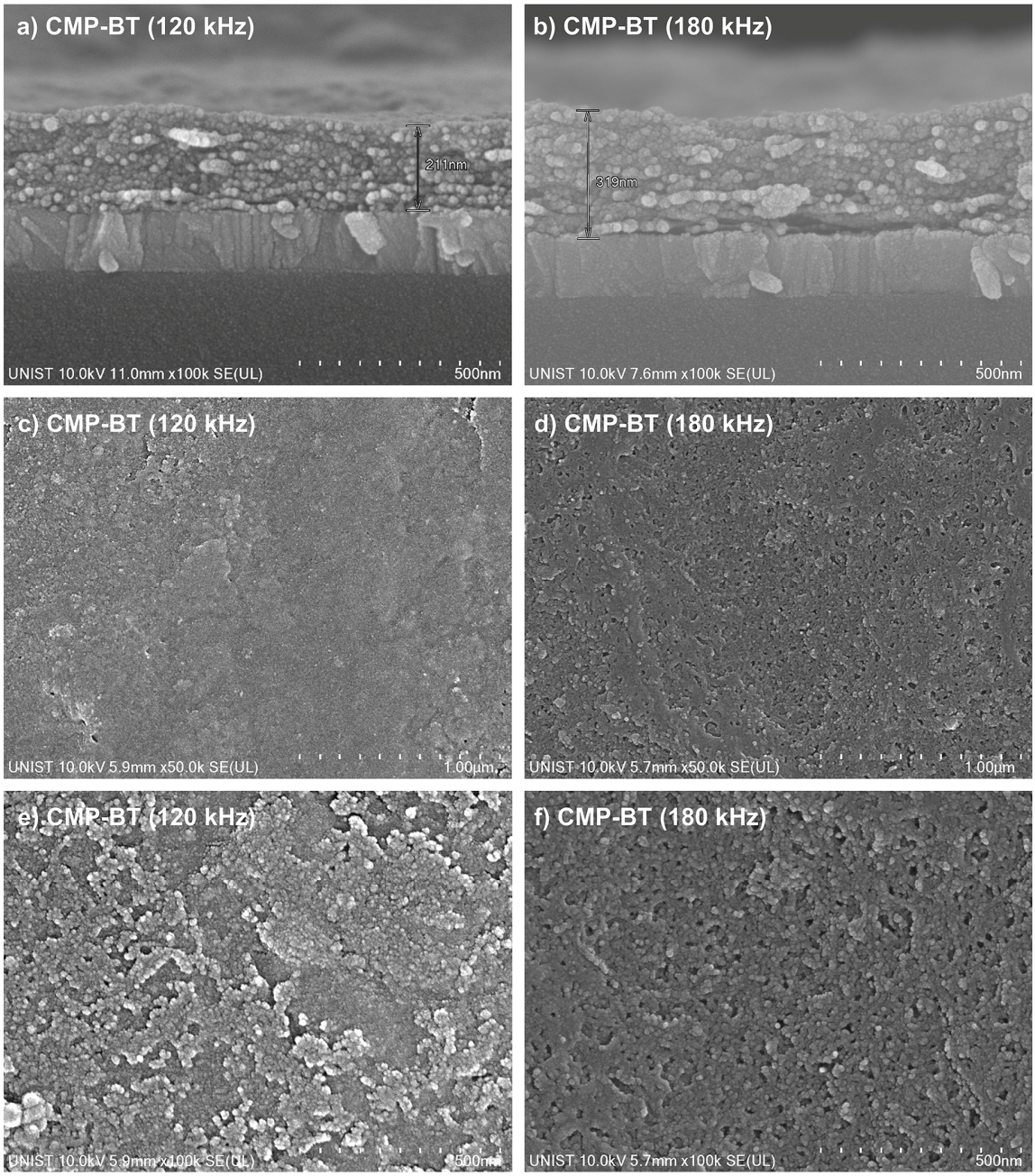

Figure S16. Cross-section SEM images of (**a**) CMP-BT (120 kHz) and (**b**) CMP-BT (180 kHz), and surface SEM images of (**c** and **e**) CMP-BT (120 kHz) and (**d** and **f**) CMP-BT (180 kHz). CMP-BT samples were fabricated on ITO glass substrates using 10 cycles of SNS.

13. Methylene blue (MB) adsorption method

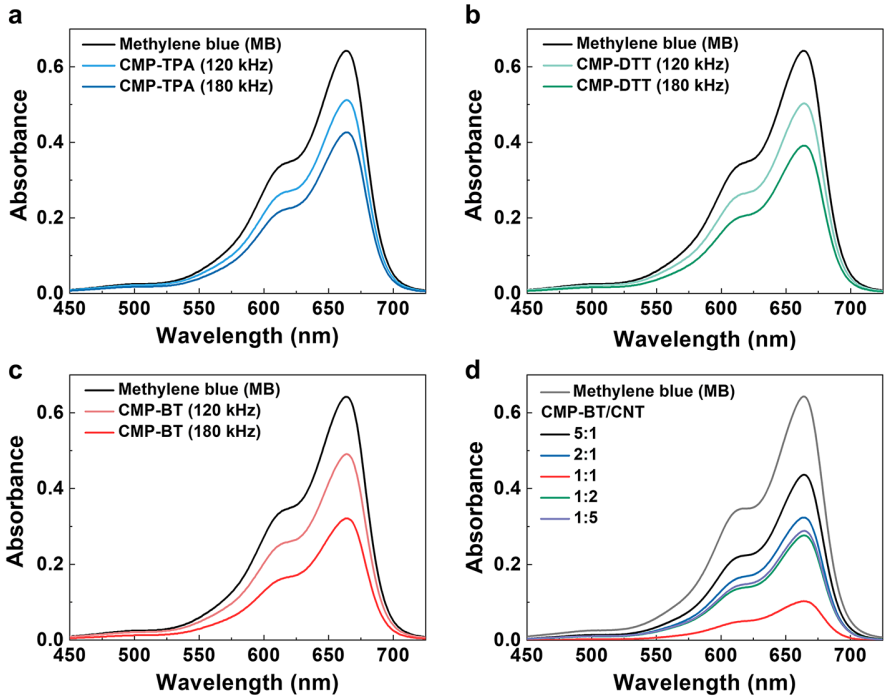

Figure S17. UV–vis spectra of initial and equilibrium methylene blue (MB) solutions of (**a**) CMP-TPA (120 and 180 kHz), (**b**) CMP-DTT (120 and 180 kHz), (**c**) CMP-BT (120 and 180 kHz), and (**d**) CMP-BT/CNT-5:1, 2:1, 1:1, 1:2, and 1:5. The concentration of the initial MB solutions was 0.01 mM in deionized water. The equilibrium MB solutions were prepared by soaking samples (2.0 cm^2) into the initial MB solutions for three days to reach maximum adsorption.

Table S5. Specific surface areas (SSA_{MB}) of electrode materials from the MB adsorption method.

Electrode material	Ultrasonic frequency (kHz)	SSA_{MB} (m^2/g)
CMP-TPA	120	219 (203 ± 13) [a]
	180	372 (356 ± 17)
CMP-DTT	120	265 (239 ± 19)
	180	336 (316 ± 17)
CMP-BT	120	329 (310 ± 16)
	180	542 (530 ± 13)
CMP-BT/CNT-5:1	180	261 (243 ± 17)
CMP-BT/CNT-2:1		404 (379 ± 18)
CMP-BT/CNT-1:1		773 (738 ± 30)
CMP-BT/CNT-1:2		463 (443 ± 19)
CMP-BT/CNT-1:5		449 (426 ± 20)

[a] Mean values ± standard deviations are shown, as obtained from four samples.

14. N_2 sorption isotherm analysis

We focused on CMP-BT because of its high SSA_{MB} and superior supercapacitor properties compared to those of CMP-DTT and CMP-TPA. N_2 sorption measurements were conducted on CMP-BT (120 and 180 kHz) powders obtained from the film-state CMP-BT to improve accuracy. As shown in Figure S18a, both CMP-BT (120 and 180 kHz) yielded combined type-I and -II N_2 sorption isotherms involving rapid N_2 sorption at low relative pressures ($P/P_0 < 0.05$) and some N_2 sorption at high relative pressures ($P/P_0 > 0.9$). Both trends can be interpreted as resulting from microporosity and inter-particulate porosity associated with the meso- and macroporosity, respectively.[12,13] In contrast, CMP-BT (ref) exhibited only a type-I isotherm. The BET specific surface areas (SSA_{BET}) and t-plot micropore areas were calculated from N_2 sorption isotherms, as listed in Table S6. CMP-BT (180 kHz) had the highest SSA_{BET} of 280 m^2/g, followed by CMP-BT (120 kHz) and CMP-BT (ref) of 180 and 110 m^2/g, respectively. This trend is consistent with the SSA_{MB} of CMP-BT (Table S5).

In particular, the microporosity contributed significantly to the SSA_{BET} considering the high micropore area; the microporosity proportions with respect to SSA_{BET} of CMP-BT (180 kHz), CMP-BT (120 kHz), and CMP-BT (ref) were ca. 79%, 72%, and 86%, respectively. Using NLDFT method, the pore size distribution (PSD) profiles of CMP-BT were obtained, revealing a narrow PSD having a dominant pore width at approximately 0.7 nm (Figure S18b), consistent with the median micropore width obtained from the Horvath–Kawazoe model (Table S6). The N_2 sorption isotherm and PSD results further confirm the predominant microporous structures of CMP-BT.

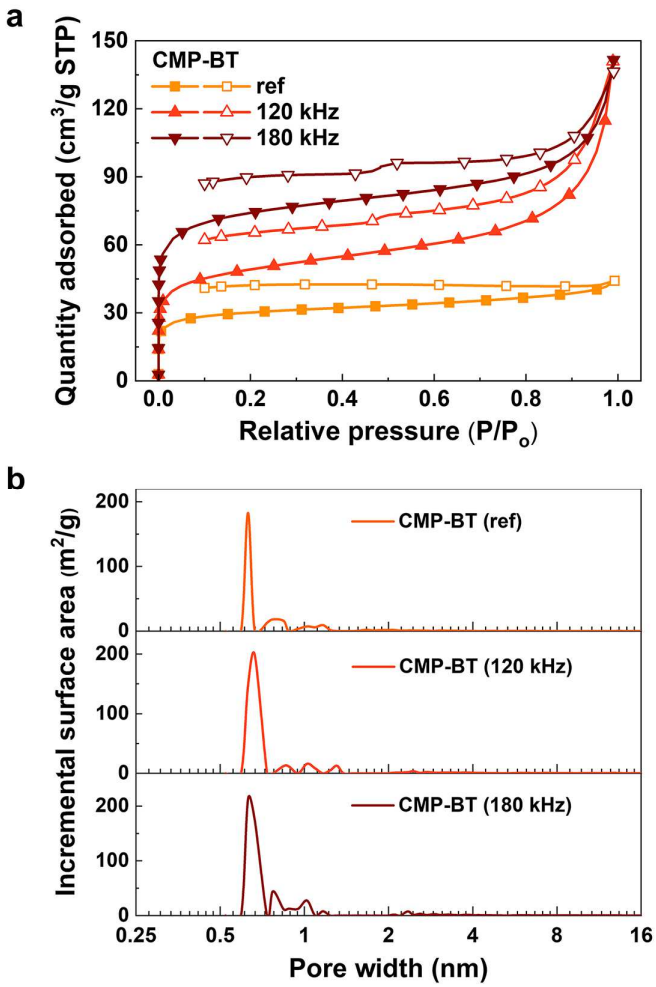

Figure S18. Porous network properties of CMP-BT. (**a**) N_2 isotherms for CMP-BT (ref, 120, and 180 kHz). The closed and open symbol mean the N_2 adsorption and desorption, respectively. (**b**) PSD curves calculated from NLDFT for CMP-BT (ref, 120, and 180 kHz).

Table S6. Summary of porosity parameters for CMP-BT with respect to the synthetic processes.

Samples	SSA_{BET} (m^2/g)	t-plot micropore area (m^2/g)	Median micropore width (nm)
CMP-BT (ref)	110	95	0.71
CMP-BT (120 kHz)	180	130	0.71
CMP-BT (180 kHz)	280	220	0.69

15. High-resolution transmission electron microscopy (HR-TEM)

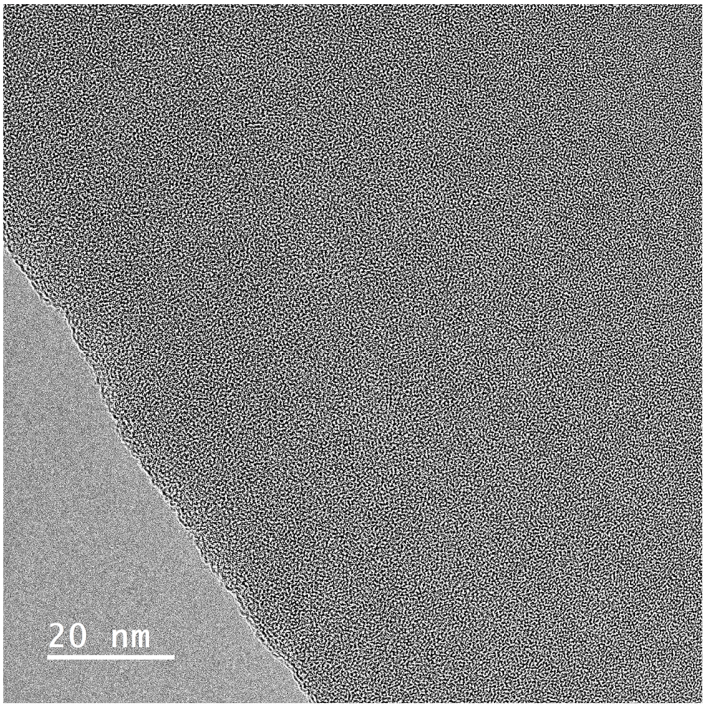

Figure S19. HR-TEM image of CMP-BT (180 kHz). Scale bar: 20 nm.

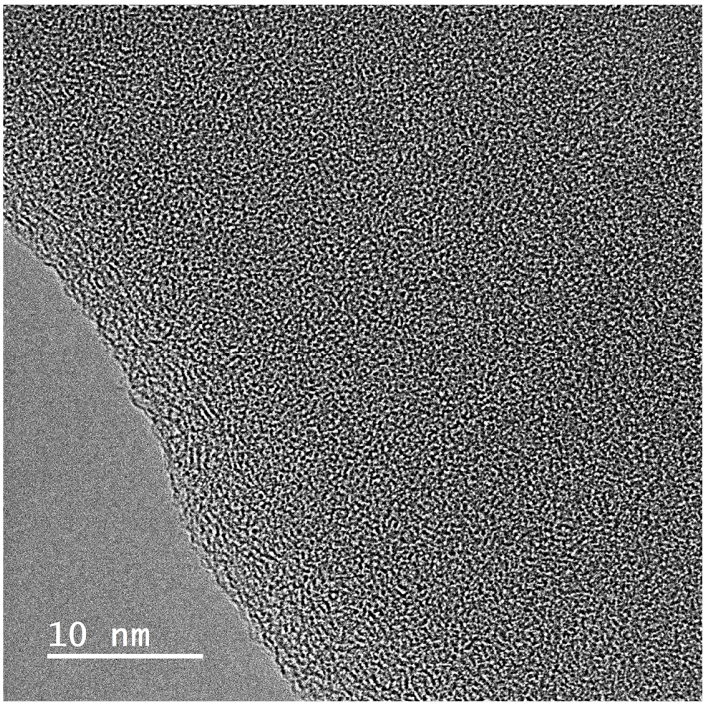

Figure S20. HR-TEM image of CMP-BT (180 kHz). Scale bar: 10 nm.

16. Electrochromic properties of CMP films

A reversible significant color change of CMP films was observed during the redox process, from the initial color of CMP films (ivory for CMP-TPA, yellow for CMP-DTT, and orange for CMP-BT) at 0 V to gray color at 1.4 V, as shown in Figures S21 and S22. The electrochromic property of CMP films was originated from the TPA unit. UV–vis–NIR absorption spectra of oxidized CMP films showed that new absorption bands appeared around 900 nm (Figures S21 and S22), characteristic of the radical cation TPA units.[14,15]

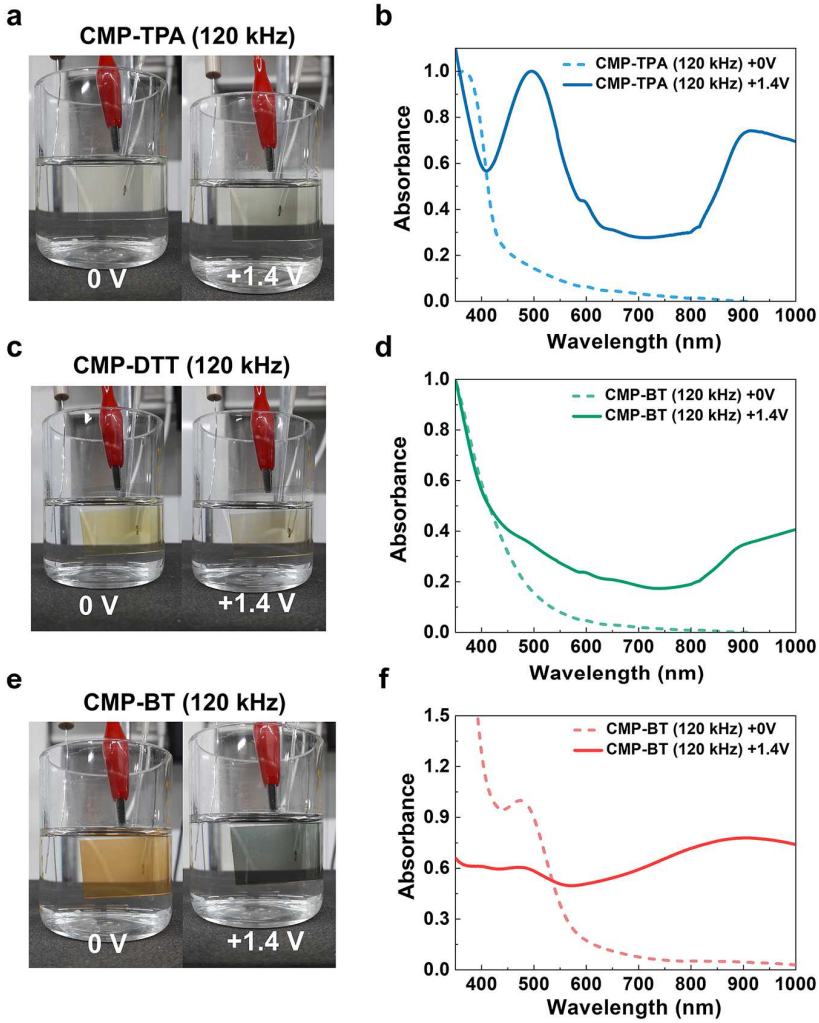

Figure S21. Photograph images and UV–vis–NIR spectra of (**a** and **b**) CMP-TPA (120 kHz), (**c** and **d**) CMP-DTT (120 kHz), and (**e** and **f**) CMP-BT (120 kHz) at 0 V and +1.4 V in a three-electrode system. Working electrode (WE): a CMP film on an ITO glass; counter electrdoe (CE): a Pt wire; reference electrode (RE): an Ag/AgCl (saturated KCl) electrode; and electrolyte: degassed 0.1 M Bu_4NPF_6 in acetonitrile.

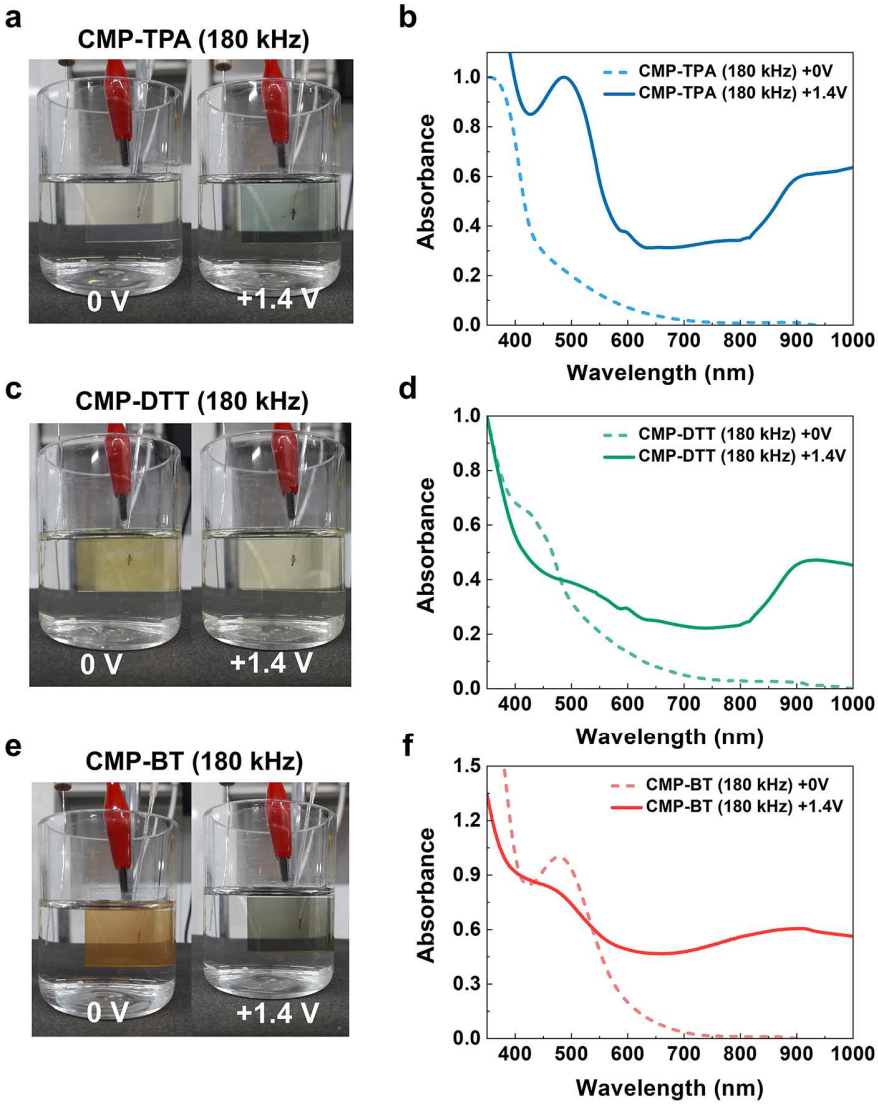

Figure S22. Photograph images and UV–vis–NIR spectra of (**a** and **b**) CMP-TPA (180 kHz), (**c** and **d**) CMP-DTT (180 kHz), and (**e** and **f**) CMP-BT (180 kHz) at 0 V and +1.4 V in a three-electrode system. WE: a CMP film on ITO glass; CE: a Pt-wire; RE: an Ag/AgCl (saturated KCl) electrode; and electrolyte: degassed 0.1 M Bu_4NPF_6 in acetonitrile.

17. Electrochemical properties of CMP films

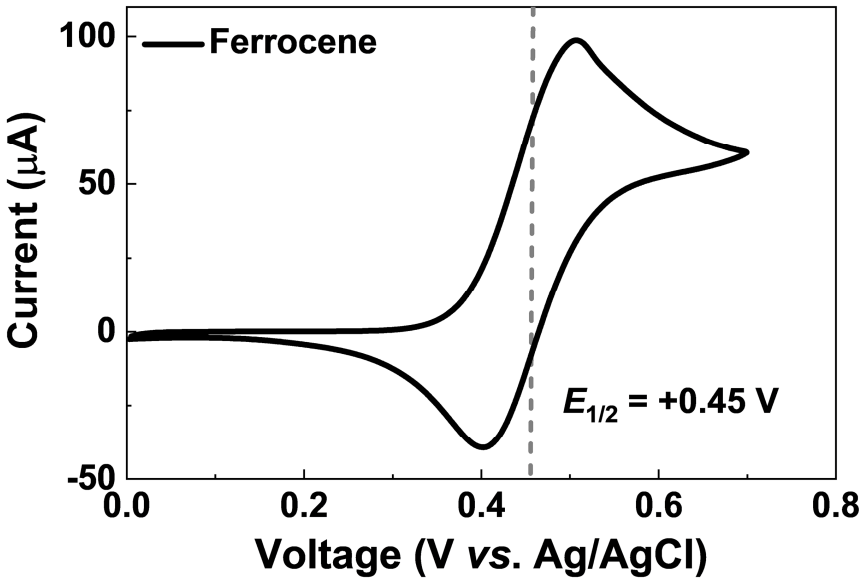

Figure S23. CV curve of ferrocene (Fc/Fc^+) at a scan rate of 10 mV/s in a three-electrode system. WE: an ITO glass; CE: a Pt wire; RE: an Ag/AgCl (saturated KCl) electrode; and electrolyte: 0.1 M Bu_4NPF_6 in acetonitrile. The measured half-wave potential ($E_{1/2}$) of Fc/Fc^+ was +0.45 V versus Ag/AgCl, which is not significantly different from the reported ferrocene redox potentials (+0.43 V versus Ag/AgCl).[16]

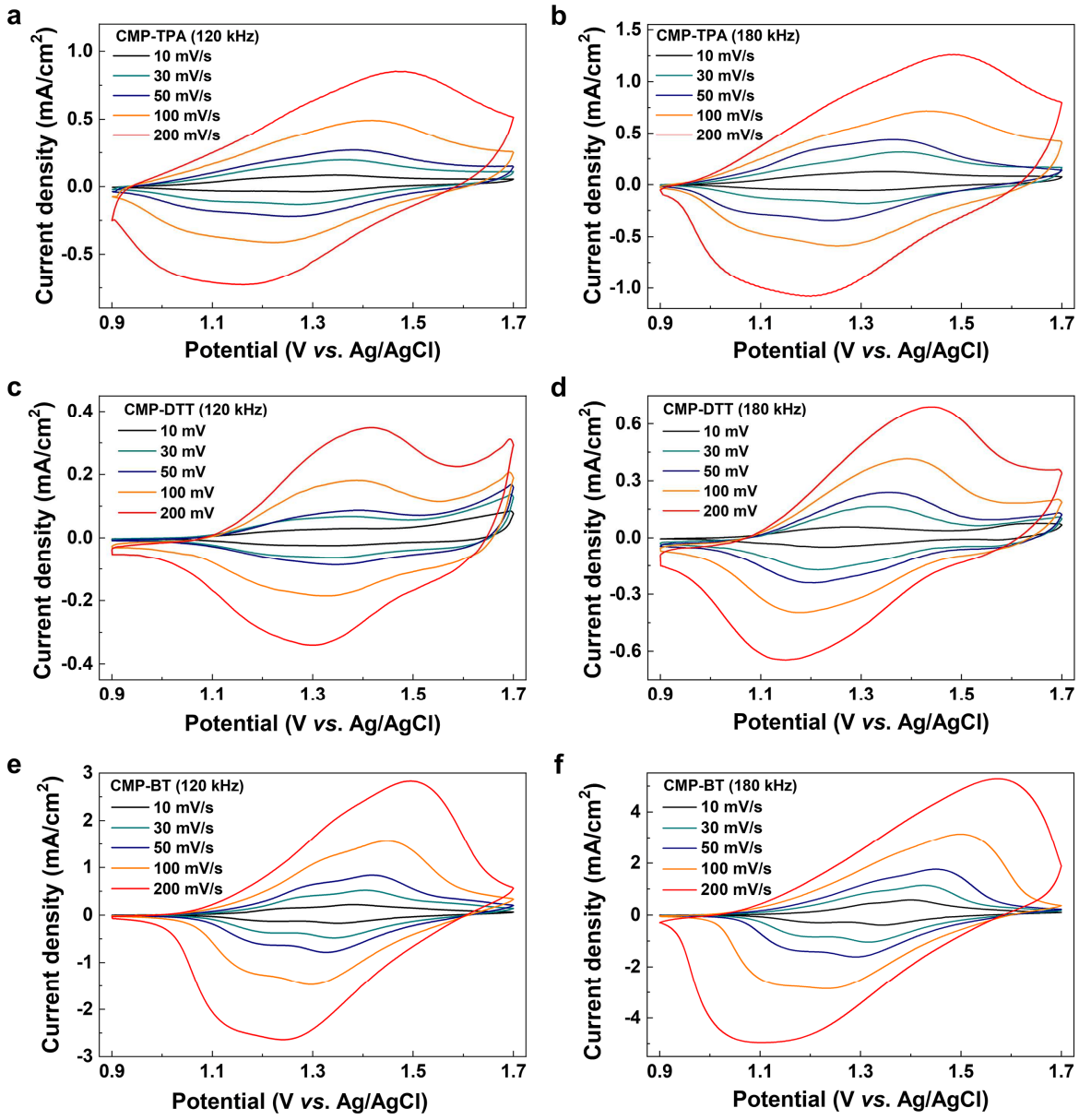

Figure S24. CV curves of areal current density versus potential for (**a**) CMP-TPA (120 kHz), (**b**) CMP-TPA (180 kHz), (**c**) CMP-DTT (120 kHz), (**d**) CMP-DTT (180 kHz), (**e**) CMP-BT (120 kHz), and (**f**) CMP-BT (180 kHz) at different scan rates (10–200 mV/s) in a three-electrode system. WE: a CMP film of 1.0 cm^2 on an ITO glass; CE: a Pt wire; RE: an Ag/AgCl (saturated KCl) electrode; and electrolyte: degassed 0.1 M Bu_4NPF_6 in acetonitrile.

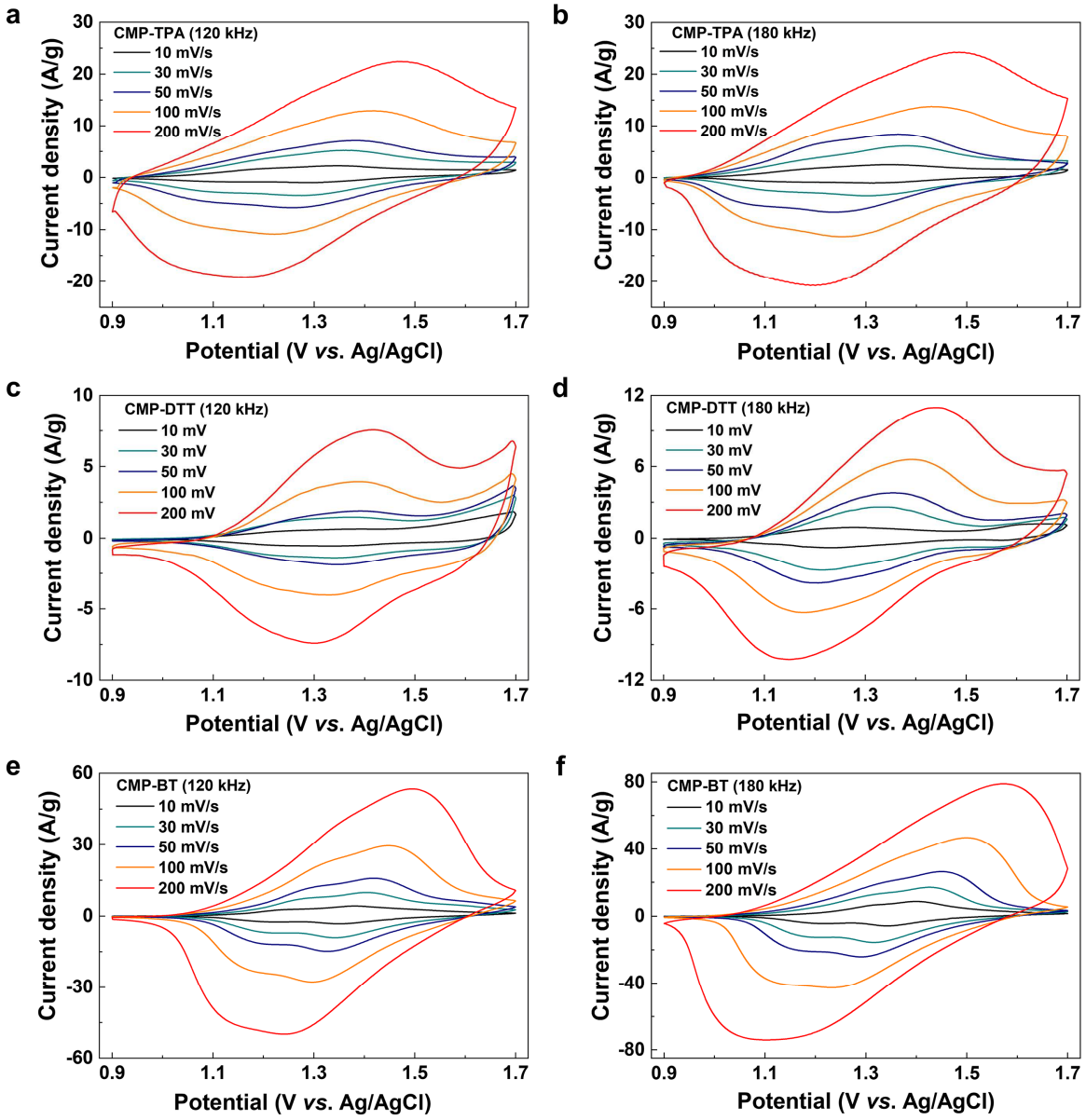

Figure S25. CV curves of gravimetric current density versus potential for (**a**) CMP-TPA (120 kHz), (**b**) CMP-TPA (180 kHz), (**c**) CMP-DTT (120 kHz), (**d**) CMP-DTT (180 kHz), (**e**) CMP-BT (120 kHz), and (**f**) CMP-BT (180 kHz) at different scan rates (10–200 mV/s) in a three-electrode system. WE: a CMP film of 1.0 cm^2 on an ITO glass; CE: a Pt wire; RE: an Ag/AgCl (saturated KCl) electrode; and electrolyte: degassed 0.1 M Bu_4NPF_6 in acetonitrile.

Table S7. Gravimetric capacitances of CMP films at different scan rates (10–200 mV/s) in a three-electrode system. WE: a CMP film of 1.0 cm^2 on an ITO glass; CE: a Pt wire; RE: an Ag/AgCl (saturated KCl) electrode; and electrolyte: degassed 0.1 M Bu_4NPF_6 in acetonitrile.

Materials	Gravimetric capacitance (F/g)					Rate capability (%) [a]
	10 mV/s	30 mV/s	50 mV/s	100 mV/s	200 mV/s	
CMP-TPA (120 kHz)	81.6 (73.6 ± 5.5) [b]	75.5 (68.1 ± 5.1)	68.9 (62.1 ± 4.6)	64.9 (58.6 ± 4.3)	57.2 (51.3 ± 4.1)	70.1
CMP-TPA (180 kHz)	91.4 (83.5 ± 6.1)	82.7 (75.5 ± 5.6)	75.4 (68.8 ± 5.1)	69.4 (63.4 ± 4.7)	62.0 (56.6 ± 4.2)	67.8
CMP-DTT (120 kHz)	45.0 (38.6 ± 5.0)	30.5 (26.2 ± 3.4)	22.6 (19.4 ± 2.4)	22.2 (19.0 ± 2.4)	19.6 (16.7 ± 2.3)	43.6
CMP-DTT (180 kHz)	49.0 (43.4 ± 4.7)	42.1 (37.3 ± 4.1)	35.9 (31.6 ± 3.8)	30.9 (27.2 ± 3.3)	26.5 (23.3 ± 2.8)	54.1
CMP-BT (120 kHz)	151 (141 ± 8)	129 (120 ± 7)	125 (117 ± 7)	120 (112 ± 7)	115 (107 ± 7)	76.5
CMP-BT (180 kHz)	251 (238 ± 11)	204 (194 ± 9)	198 (188 ± 9)	193 (183 ± 9)	187 (178 ± 8)	74.8

[a] Retention capability of specific capacitance from 10 to 200 mV/s. [b] Mean values ± standard deviations are shown, as obtained from ten samples.

Table S8. Area capacitances of CMP films at different scan rates (10–200 mV/s) in a three-electrode system. WE: a CMP film of 1.0 cm^2 on an ITO glass; CE: a Pt wire; RE: an Ag/AgCl (saturated KCl) electrode; and electrolyte: degassed 0.1 M Bu_4NPF_6 in acetonitrile.

Materials	Area capacitance (mF/cm^2)				
	10 mV/s	30 mV/s	50 mV/s	100 mV/s	200 mV/s
CMP-TPA (120 kHz)	3.10 (2.80 ± 0.21) [a]	2.87 (2.59 ± 0.19)	2.62 (2.36 ± 0.18)	2.47 (2.23 ± 0.16)	2.17 (1.95 ± 0.16)
CMP-TPA (180 kHz)	4.75 (4.34 ± 0.32)	4.30 (3.93 ± 0.29)	3.92 (3.58 ± 0.26)	3.61 (3.30 ± 0.24)	3.22 (2.94 ± 0.22)
CMP-DTT (120 kHz)	2.07 (1.78 ± 0.23)	1.40 (1.20 ± 0.15)	1.04 (0.89 ± 0.11)	1.02 (0.88 ± 0.11)	0.90 (0.77 ± 0.11)
CMP-DTT (180 kHz)	3.09 (2.74 ± 0.30)	2.65 (2.35 ± 0.26)	2.26 (1.99 ± 0.24)	1.95 (1.71 ± 0.21)	1.67 (1.47 ± 0.18)
CMP-BT (120 kHz)	8.00 (7.45 ± 0.45)	6.81 (6.35 ± 0.38)	6.63 (6.18 ± 0.37)	6.34 (5.91 ± 0.35)	6.12 (5.69 ± 0.36)
CMP-BT (180 kHz)	16.8 (15.9 ± 0.7)	13.6 (13.0 ± 0.6)	13.2 (12.6 ± 0.6)	12.9 (12.3 ± 0.6)	12.6 (11.9 ± 0.5)

[a] Mean values ± standard deviations are shown, as obtained from ten samples.

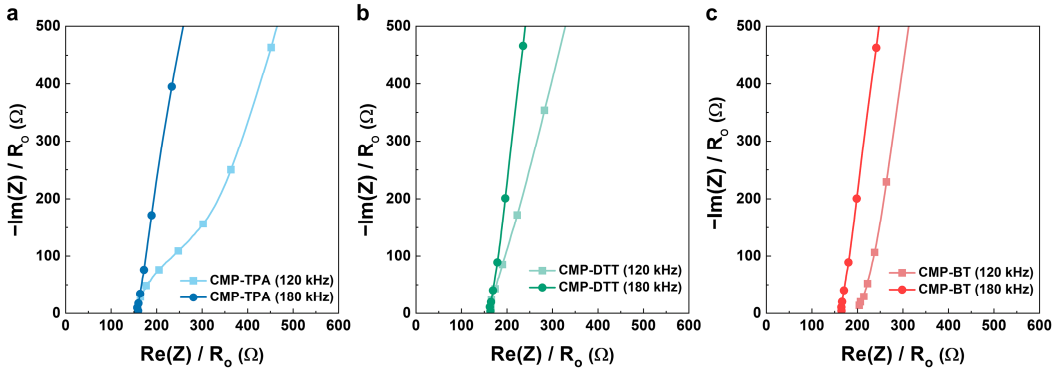

Figure S26. Nyquist plots of (**a**) CMP-TPA (120 and 180 kHz), (**b**) CMP-DTT (120 and 180 kHz), and (**c**) CMP-BT (120 and 180 kHz) in a three-electrode system. WE: a CMP film of 1.0 cm^2 on an ITO glass; CE: a Pt wire; RE: an Ag/AgCl (saturated KCl) electrode; and electrolyte: degassed 0.1 M Bu_4NPF_6 in acetonitrile. Samples were measured in the frequency range from 100 Hz to 100 kHz, and the amplitude of the AC frequency was set to 10 mV.

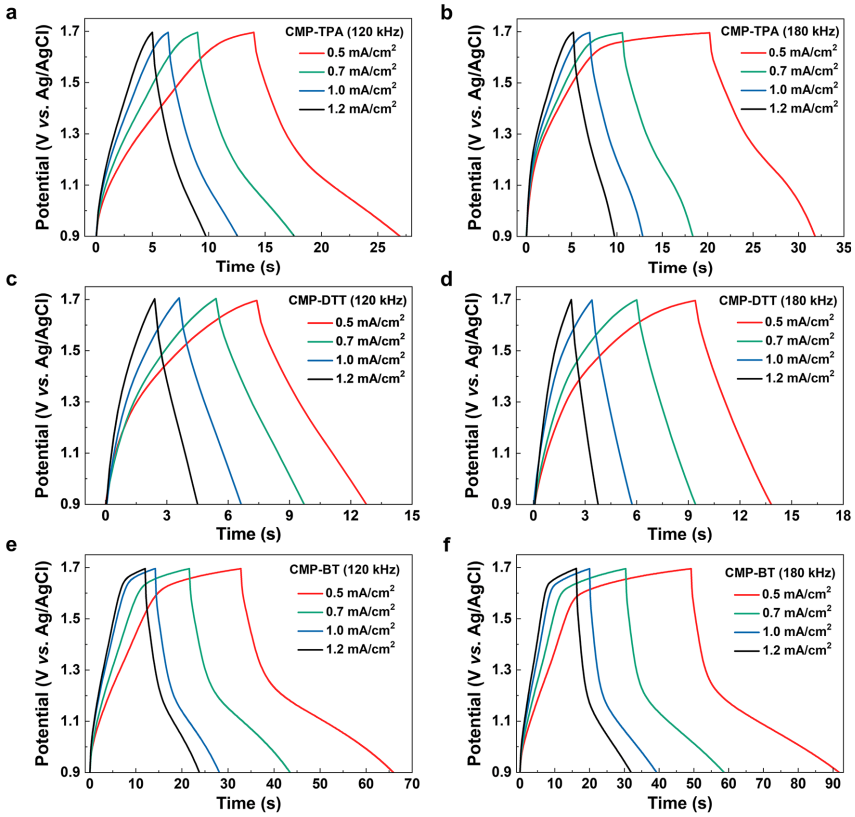

Figure S27. GCD curves of (**a**) CMP-TPA (120 kHz), (**b**) CMP-TPA (180 kHz), (**c**) CMP-DTT (120 kHz), (**d**) CMP-DTT (180 kHz), (**e**) CMP-BT (120 kHz), and (**f**) CMP-BT (180 kHz) at different current densities (0.5–1.2 mA/cm^2) in a three-electrode system. WE: a CMP film of 1.0 cm^2 on an ITO glass; CE: a Pt wire; RE: an Ag/AgCl (saturated KCl) electrode; and electrolyte: degassed 0.1 M Bu_4NPF_6 in acetonitrile. In the GCD results, the specific capacitances of CMP-BT (180 kHz), CMP-TPA (180 kHz), and CMP-DTT (180 kHz) were 19.4, 5.13, and 2.56 mF/cm^2 at a current density of 0.5 mA/cm^2, respectively.

18. Electron microscopy images of CMP-BT/CNT

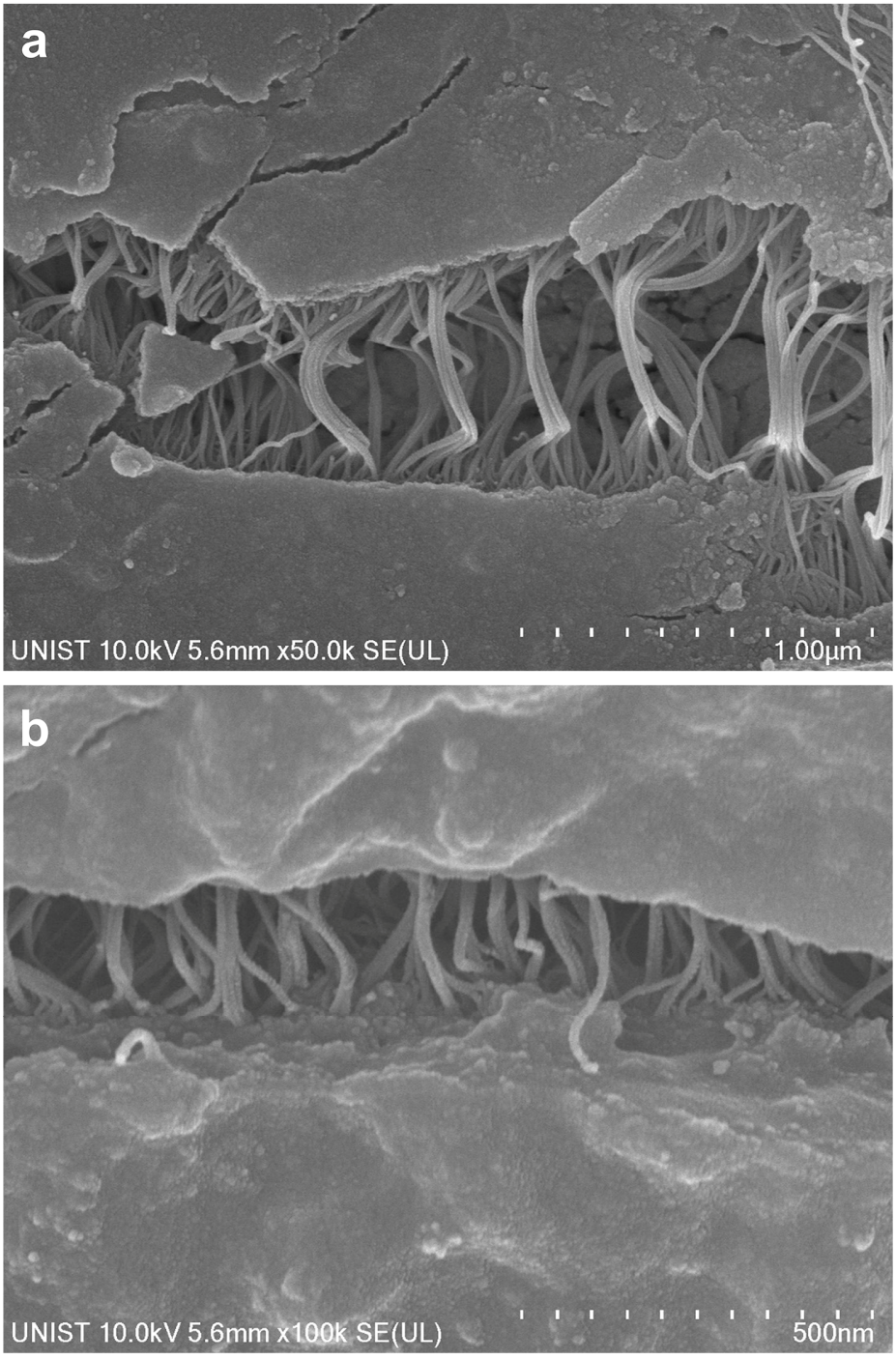

Figure S28. SEM images of CMP-BT/CNT-1:1. Scale bars: (**a**) 1.00 μm and (**b**) 500 nm.

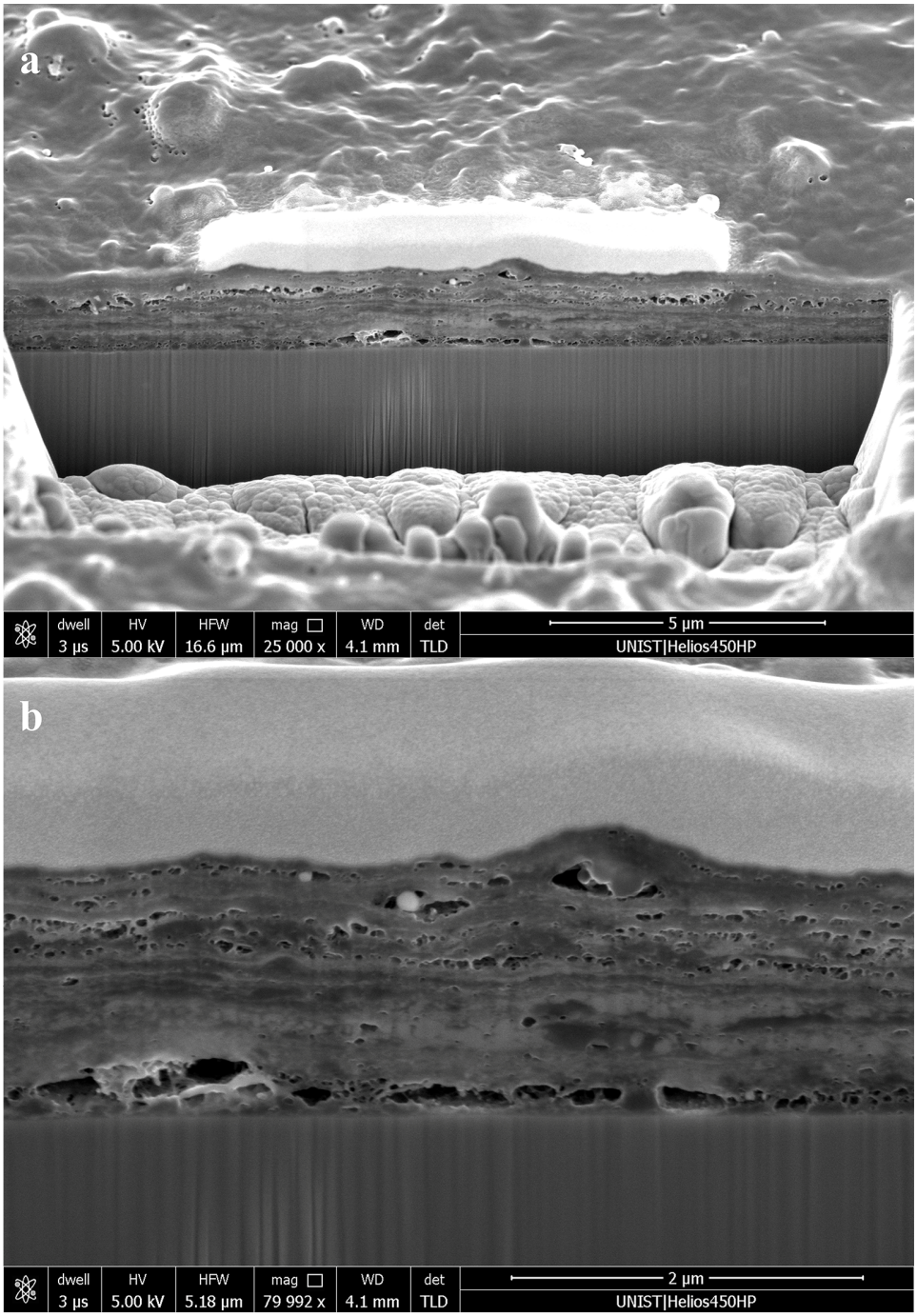

Figure S29. Cross-section SEM images of CMP-BT/CNT-1:1. Scale bars: (**a**) 5.00 μm, and (**b**) 2.00 μm.

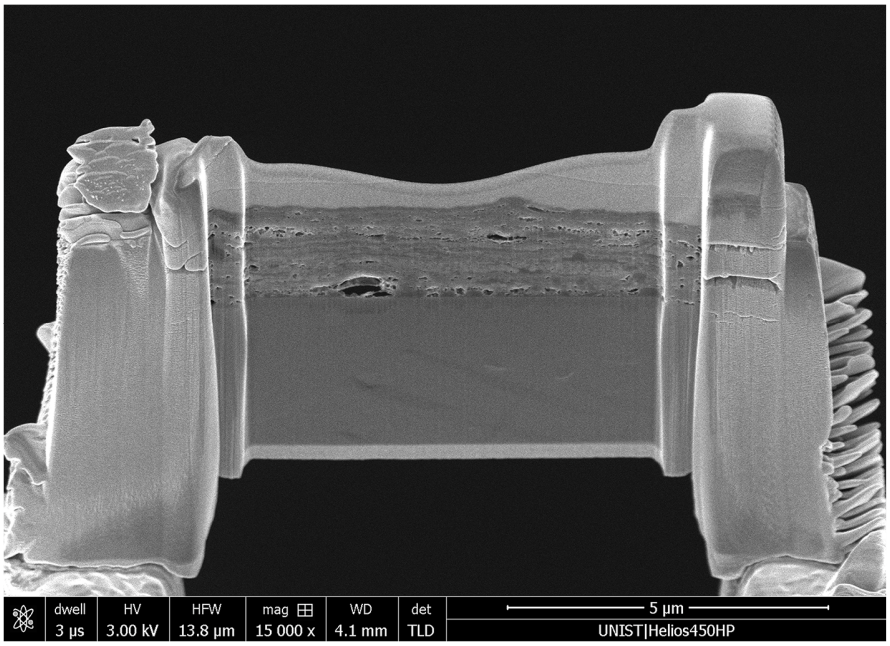

Figure S30. Cross-section SEM image of CMP-BT/CNT-1:1. Scale bar: 5.00 μm.

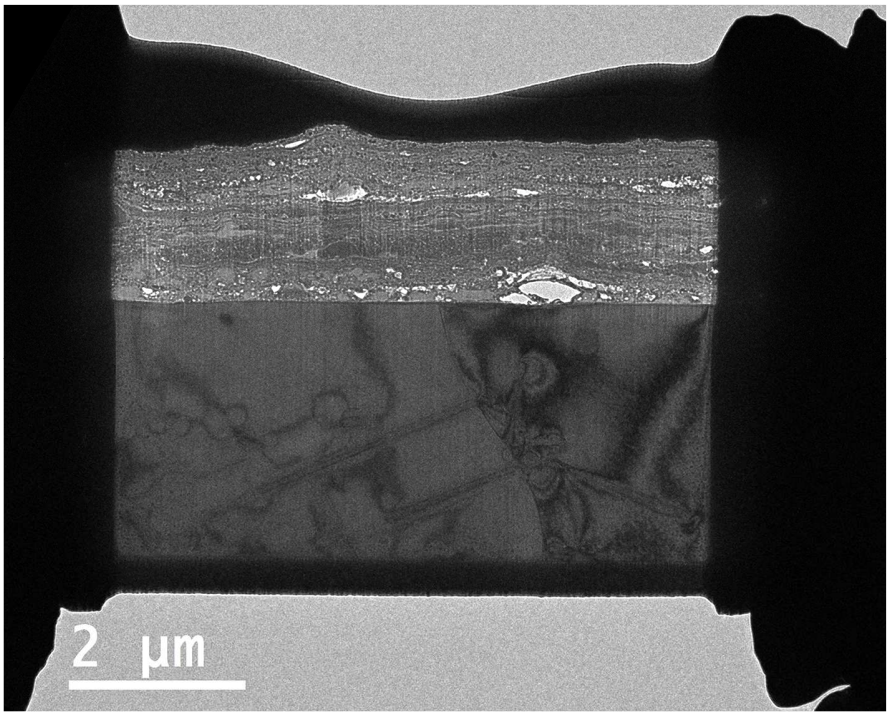

Figure S31. Cross-section HR-TEM image of CMP-BT/CNT-1:1. Scale bar: 2.00 μm.

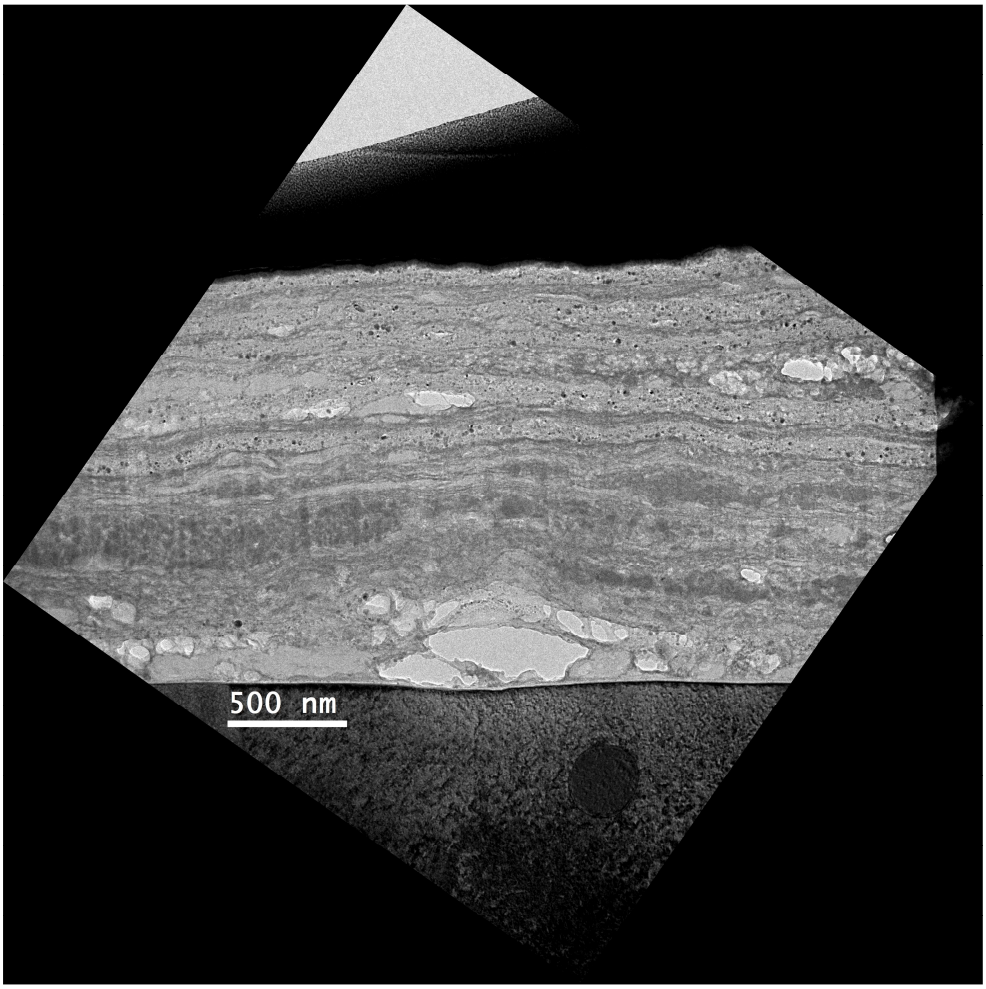

Figure S32. Cross-section HR-TEM image of CMP-BT/CNT-1:1. Scale bar: 500 nm.

19. Electrochemical properties of CMP-BT/CNT

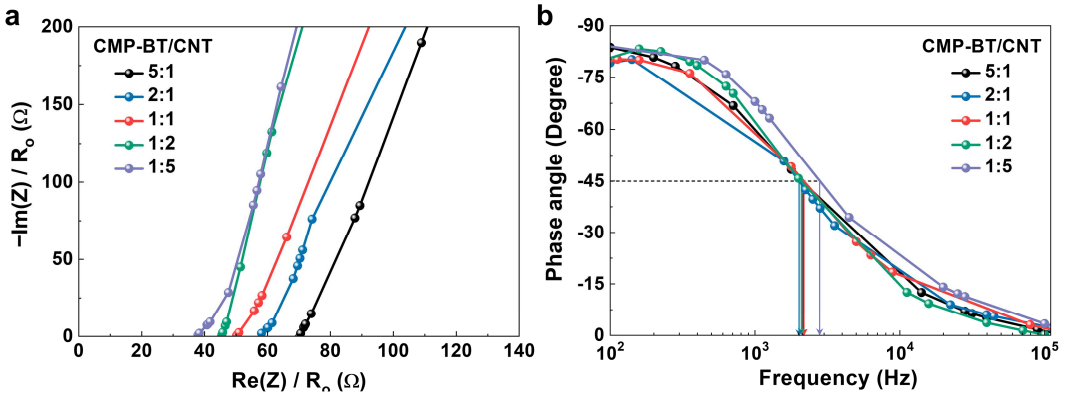

Figure S33. (**a**) Nyquist and (**b**) Bode plots of CMP-BT/CNT-5:1, 2:1, 1:1, 1:2, and 1:5 in a symmetric two-electrode system. WE and CE: CMP-BT/CNT electrodes of 1.0 cm^2 on Ti-foil; and electrolyte: 0.1 M Bu_4NPF_6 in acetonitrile. Samples were measured in the frequency range from 100 Hz to 100 kHz, and the amplitude of the AC frequency was set to 10 mV.

Table S9. Electrochemical impedance spectroscopy results of CMP-BT/CNT-5:1, 2:1, 1:1, 1:2, and 1:5 in a symmetric two-electrode system. WE and CE: CMP-BT/CNT electrodes of 1.0 cm^2 on Ti-foil; and electrolyte: 0.1 M Bu_4NPF_6 in acetonitrile.

CMP-BT:CNT ratio	Equivalent series resistance (Ω) [a]	Relaxation time (τ_0, ms) [b]
5:1	71	0.57
2:1	58	0.63
1:1	50	0.56
1:2	45	0.56
1:5	38	0.34

[a] Equivalent series resistances were calculated from the *x*-intercept of the Nyquist plots. [b] Relaxation times were calculated from $\tau_0 = 1/f_0$, where f_0 is the characteristic frequency at a phase angle of −45° in the Bode plots.

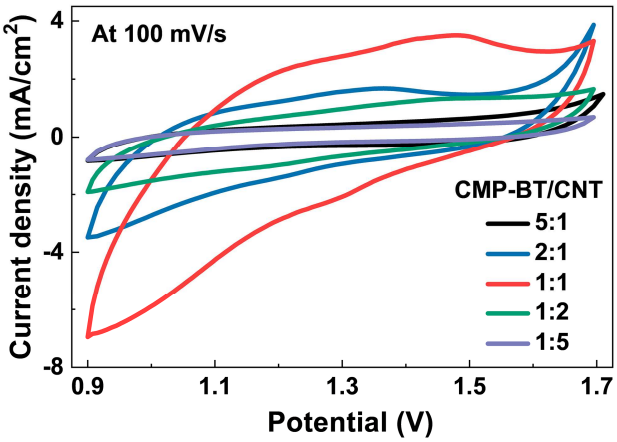

Figure S34. CV curves of areal current density versus potential for CMP-BT/CNT (5:1, 2:1, 1:1, 1:2, and 1:5) at a scan rate of 100 mV/s in a symmetric two-electrode system. WE and CE: CMP-BT/CNT electrodes of 1.0 cm^2 on Ti-foil; and electrolyte: 0.1 M Bu_4NPF_6 in acetonitrile.

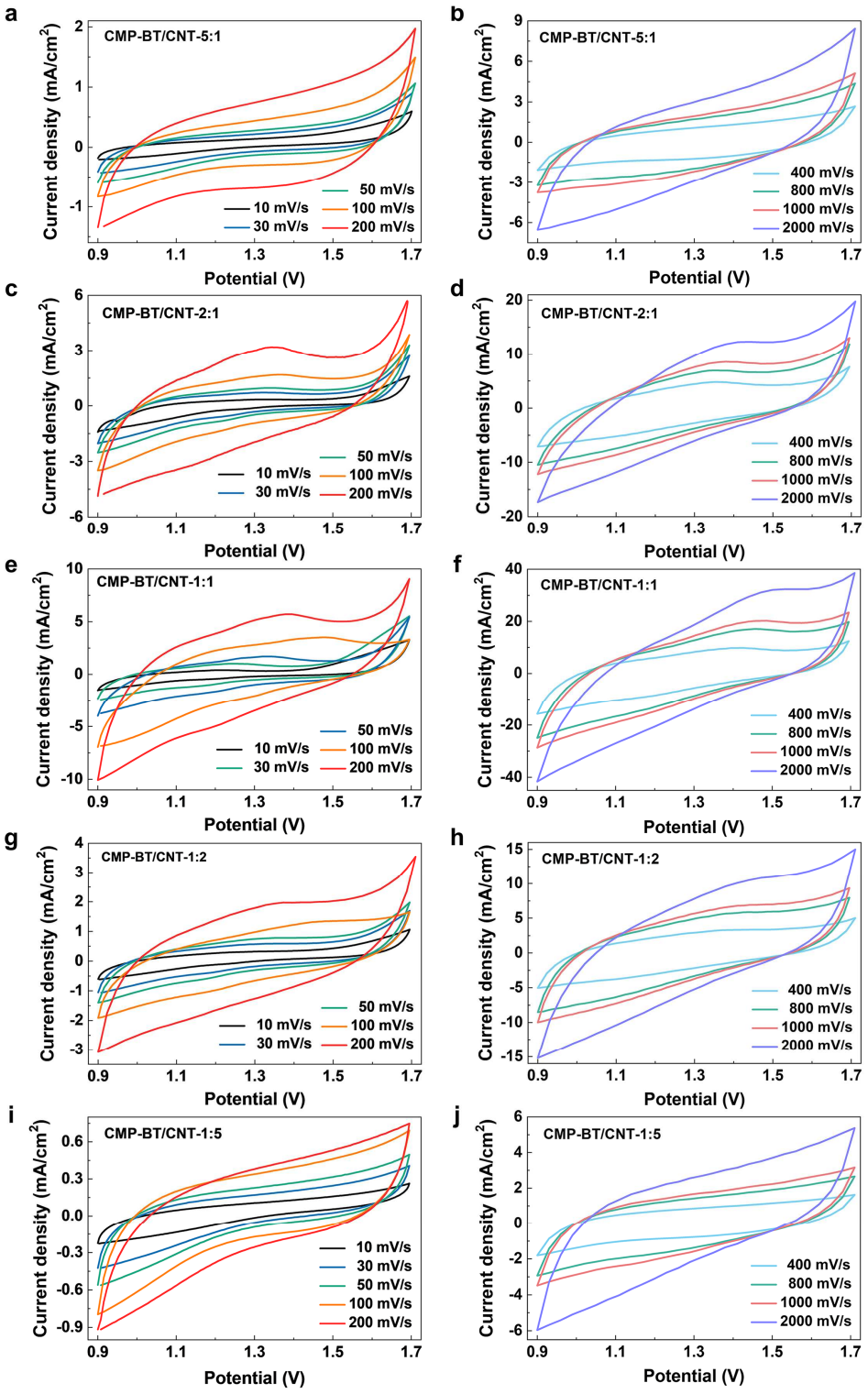

Figure S35. CV curves of areal current density versus potential for CMP-BT/CNT (**a** and **b**) 5:1, (**c** and **d**) 2:1, (**e** and **f**) 1:1, (**g** and **h**) 1:2, and (**i** and **j**) 1:5 at different scan rates (10–2000 mV/s) in a symmetric two-electrode system. WE and CE: CMP-BT/CNT electrodes of 1.0 cm^2 on Ti-foil; and electrolyte: 0.1 M Bu_4NPF_6 in acetonitrile.

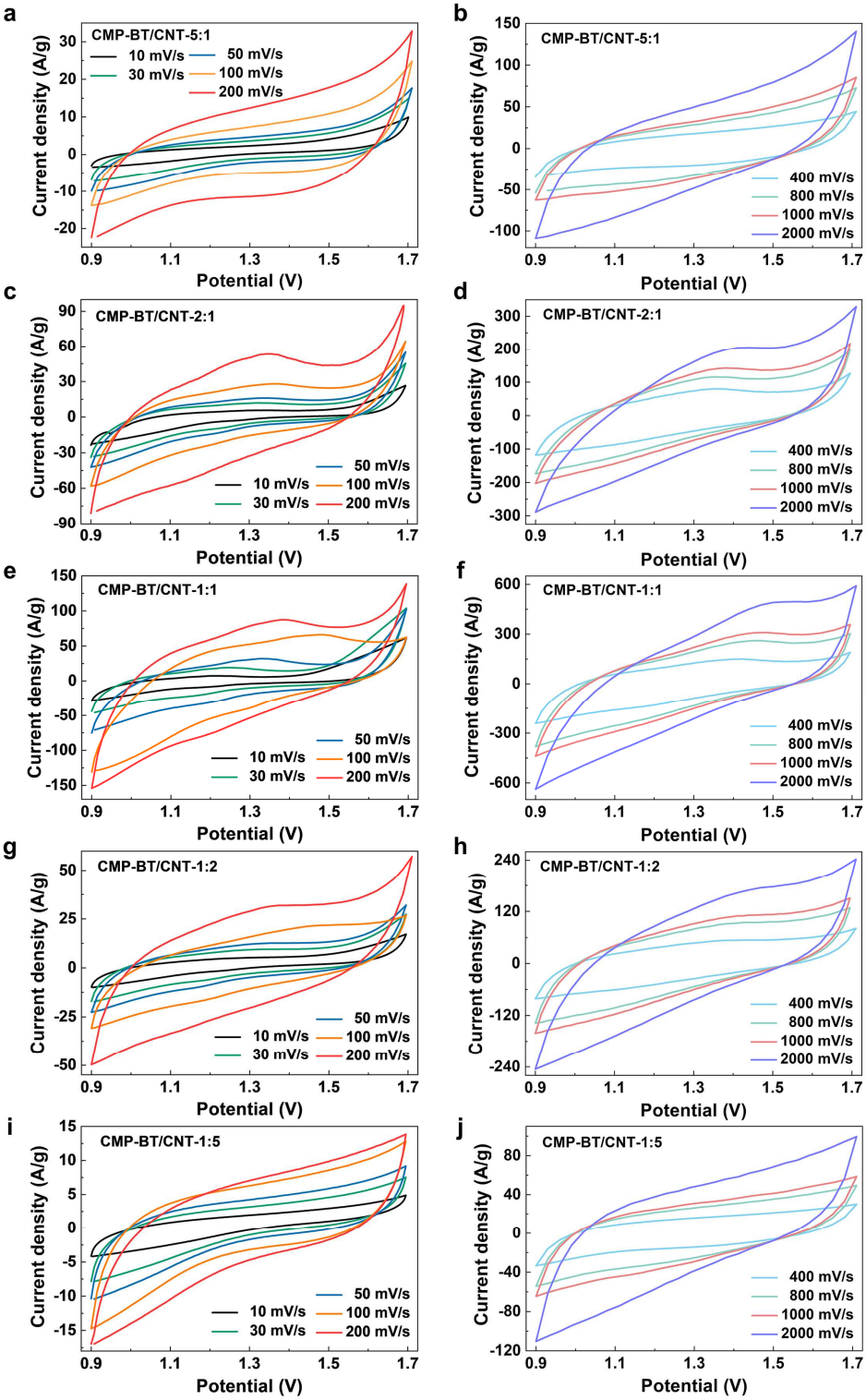

Figure S36. CV curves of gravimetric current density versus potential for CMP-BT/CNT (**a** and **b**) 5:1, (**c** and **d**) 2:1, (**e** and **f**) 1:1, (**g** and **h**) 1:2, and (**i** and **j**) 1:5 at different scan rates (10–2000 mV/s) in a symmetric two-electrode system. WE and CE: CMP-BT/CNT electrodes of 1.0 cm^2 on Ti-foil; and electrolyte: 0.1 M Bu_4NPF_6 in acetonitrile.

Table S10. Area capacitances of CMP-BT/CNT-5:1, 2:1, 1:1, 1:2, and 1:5 at different scan rates (10–2000 mV/s) in a symmetric two-electrode system. WE and CE: CMP-BT/CNT electrodes of 1.0 cm^2 on Ti-foil; and electrolyte: 0.1 M Bu_4NPF_6 in acetonitrile.

CMP-BT :CNT ratio	Specific area capacitance (mF/cm^2) [a]								
	10 mV/s	30 mV/s	50 mV/s	100 mV/s	200 mV/s	400 mV/s	800 mV/s	1000 mV/s	2000 mV/s
5:1	18.2 (16.3 ± 1.5)	11.7 (10.4 ± 1.1)	7.88 (6.98 ± 0.76)	5.72 (5.07 ± 0.55)	4.03 (3.57 ± 0.39)	3.23 (2.86 ± 0.31)	2.40 (2.13 ± 0.23)	2.18 (1.93 ± 0.21)	1.51 (1.34 ± 0.15)
2:1	38.4 (35.6 ± 2.2)	24.6 (22.8 ± 1.4)	23.5 (21.8 ± 1.3)	14.6 (13.5 ± 0.8)	12.2 (11.3 ± 0.7)	9.50 (8.80 ± 0.54)	7.25 (6.72 ± 0.41)	6.44 (5.97 ± 0.37)	3.71 (3.44 ± 0.21)
1:1	61.3 (58.6 ± 2.1)	44.7 (42.7 ± 1.6)	40.3 (38.5 ± 1.4)	36.2 (34.6 ± 1.3)	26.5 (25.3 ± 0.9)	21.2 (20.3 ± 0.7)	16.5 (15.8 ± 0.6)	14.7 (14.0 ± 0.5)	9.40 (8.98 ± 0.33)
1:2	21.5 (19.5 ± 1.4)	17.3 (15.7 ± 1.1)	14.4 (13.0 ± 0.9)	9.21 (8.33 ± 0.59)	8.60 (7.78 ± 0.55)	6.75 (6.11 ± 0.43)	5.51 (4.71 ± 0.33)	4.94 (4.47 ± 0.32)	3.25 (2.94 ± 0.21)
1:5	7.21 (6.59 ± 0.48)	5.67 (5.18 ± 0.38)	5.16 (4.71 ± 0.35)	4.62 (4.22 ± 0.31)	2.81 (2.56 ± 0.19)	2.24 (2.05 ± 0.15)	1.96 (1.79 ± 0.13)	1.83 (1.67 ± 0.12)	1.70 (1.56 ± 0.11)

[a] Mean values ± standard deviations in parenthesis are shown, as obtained from ten samples.

Table S11. Gravimetric capacitance of CMP-BT/CNT-5:1, 2:1, 1:1, 1:2, and 1:5 at different scan rates (10–2000 mV/s) in a symmetric two-electrode system. WE and CE: CMP-BT/CNT electrodes of 1.0 cm^2 on Ti-foil; and electrolyte: 0.1 M Bu_4NPF_6 in acetonitrile.

CMP-BT :CNT ratio	Specific gravimetric capacitance (F/g) [a]								
	10 mV/s	30 mV/s	50 mV/s	100 mV/s	200 mV/s	400 mV/s	800 mV/s	1000 mV/s	2000 mV/s
5:1	205 (183 ± 17)	132 (117 ± 13)	88.6 (78.5 ± 8.6)	64.3 (57.0 ± 6.2)	45.3 (40.1 ± 4.4)	36.3 (32.2 ± 3.5)	27.0 (23.9 ± 2.6)	24.5 (21.7 ± 2.4)	17.0 (15.1 ± 1.6)
2:1	449 (416 ± 25)	288 (266 ± 16)	275 (255 ± 16)	171 (158 ± 10)	143 (132 ± 8)	111 (103 ± 6)	84.7 (78.5 ± 4.8)	75.3 (69.8 ± 4.3)	43.4 (40.2 ± 2.5)
1:1	756 (722 ± 26)	551 (526 ± 19)	497 (475 ± 17)	446 (426 ± 16)	327 (312 ± 11)	261 (250 ± 9)	203 (194 ± 7)	181 (173 ± 6)	116 (111 ± 4)
1:2	265 (240 ± 17)	213 (193 ± 14)	178 (161 ± 11)	114 (103 ± 7)	106 (96 ± 7)	83.2 (75.3 ± 5.3)	64.2 (58.1 ± 4.1)	60.9 (55.1 ± 3.9)	40.1 (36.3 ± 2.6)
1:5	84.3 (77.0 ± 5.6)	66.3 (60.6 ± 4.4)	60.3 (55.1 ± 4.0)	54.0 (49.3 ± 3.6)	32.8 (30.0 ± 2.2)	26.2 (23.9 ± 1.8)	22.9 (20.9 ± 1.5)	21.4 (19.5 ± 1.4)	19.9 (18.2 ± 1.3)

[a] Mean values ± standard deviations in parenthesis are shown, as obtained from ten samples.

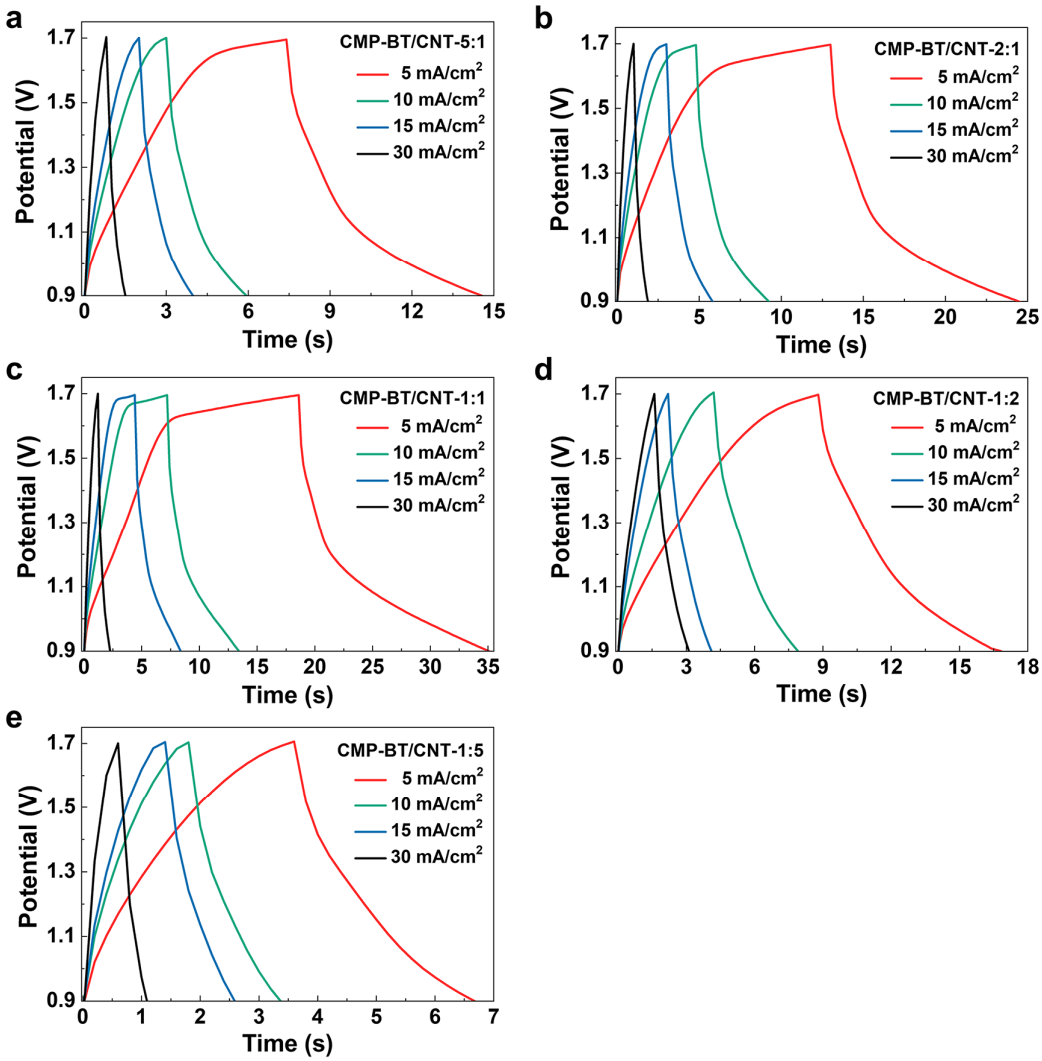

Figure S37. GCD curves of CMP-BT/CNT (**a**) 5:1, (**b**) 2:1, (**c**) 1:1, (**d**) 1:2, and (**e**) 1:5 at different current densities (5–30 mA/cm^2) in a symmetric two-electrode system. WE and CE: CMP-BT/CNT electrodes of 1.0 cm^2 on Ti-foil; and electrolyte: 0.1 M Bu_4NPF_6 in acetonitrile.

We simultaneously injected both the monomer precursor and CNT dispersion in one SNS process (i.e., co-deposition) for comparison. As shown in Figure S38, the CMP-BT/CNT electrodes prepared using co-deposition (CD) showed more aggregated and less porous morphology than the CMP-BT/CNT fabricated using layer-by-layer (LBL) deposition because precipitates would be formed when the two solutions were mixed at ultrasonic nozzle in the CD process owing to their antisolvent conditions to each other [monomer precursor–chloroform/ethanol (*v*/*v* = 1:1) and CNT dispersion–water/ethanol (*v*/*v* = 1:1)]. As the result of morphological differences, the capacitive performance of CMP-BT/CNT (CD) was much lower than that of CMP-BT/CNT (LBL), as shown in Figure S38c. For these reasons, we optimized the LBL structure of CMP-BT/CNT through SNS process, and this approach enhanced specific surface areas and capacitive performances of CMP-based electrodes.

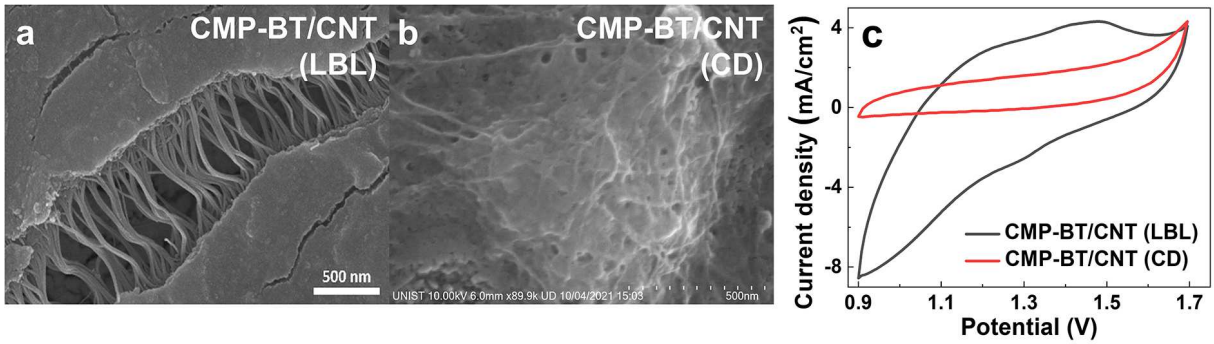

Figure S38. SEM images of CMP-BT/CNT electrodes prepared using (**a**) layer-by-layer (LBL) and (**b**) co-deposition (CD) in SNS process. In the CD process, the monomer precursor, CNT dispersion, and spray parameters (the nozzle-to-substrate distance, speed of spray-head, flow rate, pressure of N_2 gas, and temperature of substrate) were identical to those of the LBL process. (**c**) CV curves of CMP-BT/CNT (LBL and CD) at a scan rate of 100 mV/s in a symmetric two-electrode systems. WE and CE: CMP-BT/CNT of 1.0 cm^2 on Ti-foil; and electrolyte: degassed 0.1 M Bu_4NPF_6 in acetonitrile.

20. Electrochemical properties of CNT electrode as a control sample

To verify the contribution of the CNTs to the supercapacitor performance of CMP-BT/CNT, we fabricated a CNT electrode and measured its capacitance as a control sample. The CNT electrode was fabricated on Ti-foil (1.0 cm^2) using 10 cycles of SNS with the CNT dispersion (0.50 mg/mL), that is the same amount of CNTs as in CMP-BT/CNT-1:1. In Figure S39a, the CV curves of CNT showed a rectangular shape consistent with electrical double layer capacitor (EDLC) behavior at different scan rates (10–100 mV/s). The CNT electrode exhibited a gravimetric capacitance of 97.7 F/g at 10 mV/s and a rate capability of 44.8% from 10 to 100 mV/s, which are lower capacitances than those of CMP-BT (180 kHz) and CMP-BT/CNT-1:1 (Figure S39b). This is because the CNT electrode suffers from re-agglomeration.[17]

However, when we introduced CNTs into the CMP-BT electrode as layer-by-layer structures using SNS, the CMP-BT/CNT-1:1 showed enhanced supercapacitor performance with robust cycling stability (Figure 4c,e). In addition, the potential window of CMP-BT/CNT-1:1 was 0.9–1.7 V, which is different from the potential window (0–1.0 V) of the CNT electrode. Therefore, the enhanced capacitance of CMP-BT/CNT-1:1 is a result of the inserted CNT layers increasing the electrical conductivity (Figure 4d) and SSA_{MB} (Table S5) of the supercapacitor electrode.

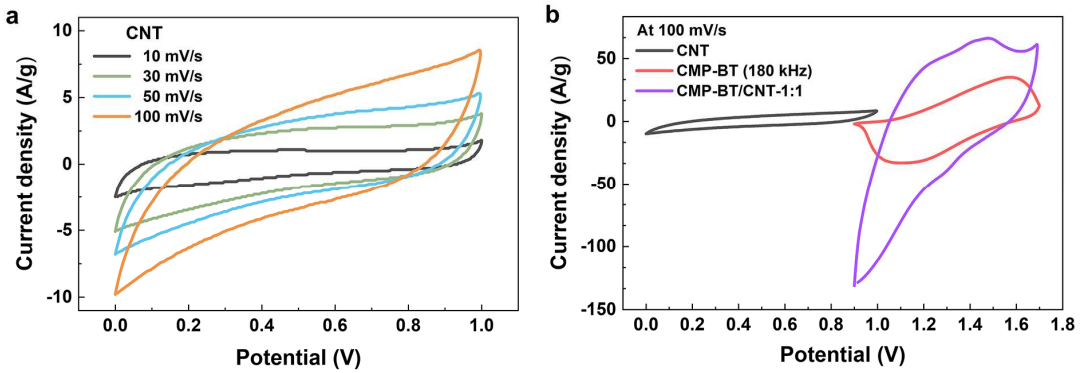

Figure S39. (**a**) CV curves of CNT at different scan rates (10–100 mV/s) in a symmetric two-electrode system. (**b**) CV curves of CNT, CMP-BT (180 kHz), and CMP-BT/CNT-1:1 at a scan rate of 100 mV/s in a symmetric two-electrode system. WE and CE electrodes were fabricated on Ti-foil with 1.0 cm^2. All electrochemical measurements were performed in degassed acetonitrile containing 0.1 M Bu_4NPF_6.

21. Ragone plots

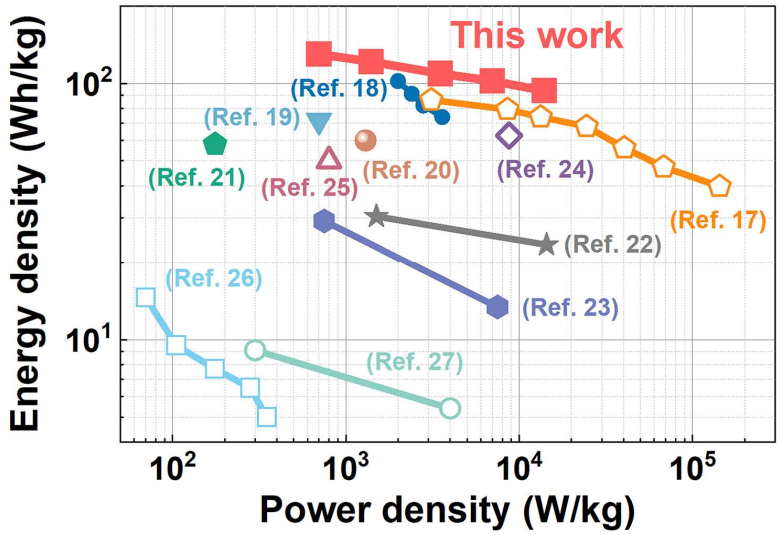

Figure S40. Ragone plots of CMP-BT/CNT//RGO/CNT and the reported supercapacitors using organic materials (Table S12). Filled and open symbols indicate asymmetric and symmetric supercapacitors, respectively.

22. Comparison of supercapacitor performance

Table S12. Comparison of electrochemical performances for CMP-BT/CNT//RGO/CNT with the reported symmetric and asymmetric supercapacitors using organic materials.

Materials (Systems)	Potential window (V)	Capacitance (F/g)	Current density (A/g)	Energy density (Wh/kg)	Power density (W/kg)	Electrolyte	Ref
CMP-BT/CNT // RGO/CNT (Asymmetric)	1.4	477	1	130	700	0.1 M Bu_4NP_6 in acetonitrile	This work
		446	2	121	1400		
		401	5	110	3500		
		375	10	102	7000		
		344	20	94	14000		
N-RGO/N-CNT (Symmetric)	1.0	621	10 mV/s	86	3110	3.0 M H_2SO_4	[17]
		570	30 mV/s	79	8560		
		532	50 mV/s	74	13300		
		489	100 mV/s	68	24500		
		404	200 mV/s	56	40400		
		341	400 mV/s	47	68100		
		286	1000 mV/s	40	143000		
NENP-1 // AC (Asymmetric)	1.6	287	5	102	2000	0.1 M H_2SO_4	[18]
		255	6	91	2400		
		230	7	82	2800		
		210	8	74	3600		
CNT/NKCOF-2 // AC (Asymmetric)	1.4	238	1	71	700	PVA-H_2SO_4 gel	[19]
PTAQTA // AC (Asymmetric)	1.6	168	1	60	1300	0.5 M H_2SO_4	[20]
Poly(1,5-NAPD) // Poly(4,4′-ODA) (Asymmetric)	1.6	165	0.2	58	176	1.0 M H_2SO_4	[21]
PCQTH // PEDOT:PSS (Asymmetric)	3.0	-	1	30.4	1500	0.5 M $TEABF_4$ in propylene carbonate	[22]
		-	10	23.6	14400		
PDC-MA/COF // AC (Asymmetric)	1.5	94	1	29.2	750	6.0 M KOH	[23]
		43	10	13.5	7500		
PTF-700 (Symmetric)	3.5	~150	0.5	62.7	8750	[EMIM][BF_4]	[24]
B/NG (Symmetric)	1.6	630	5 mV/s	50	800	2.0 M Li_2SO_4	[25]
TaPa-$(OH)_2$ (Symmetric)	0.7	214	0.2	14.6	70	1.0 M Phosphate buffer (pH = 7.2)	[26]
		139	0.3	9.5	105		
		113	0.5	7.7	175		
		96	0.8	6.5	280		
		73	1	5.0	350		
TaPa-Py-COF (Symmetric)	0.8	102	0.5	9.1	300	1.0 M H_2SO_4	[27]
		61	10	5.4	4000		

23. Nuclear magnetic resonance (NMR) spectra of materials

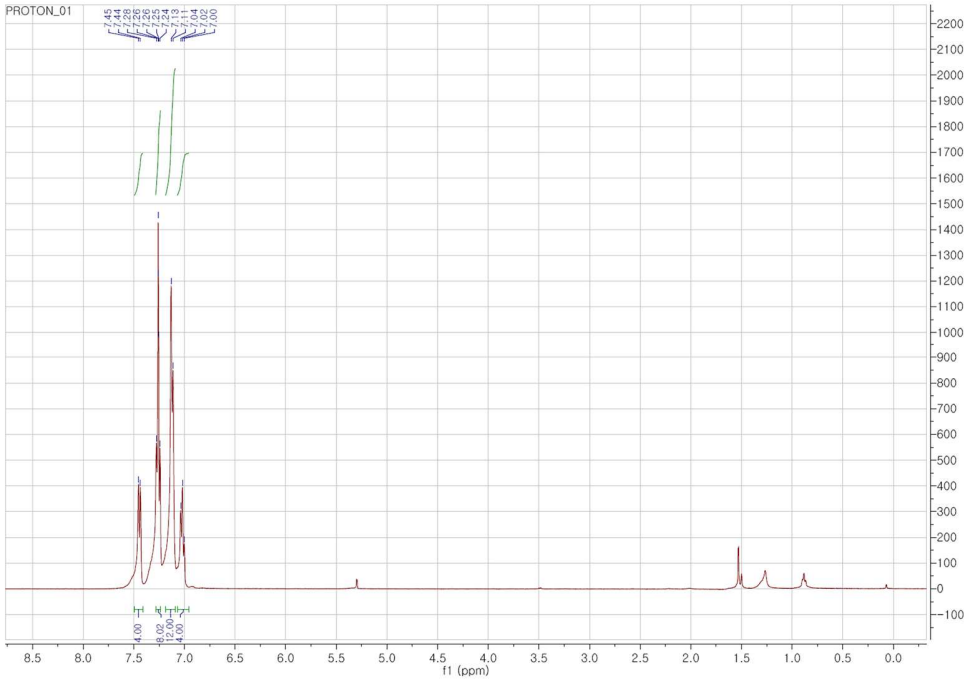

Figure S41. ^{1}H-NMR spectrum of M-TPA

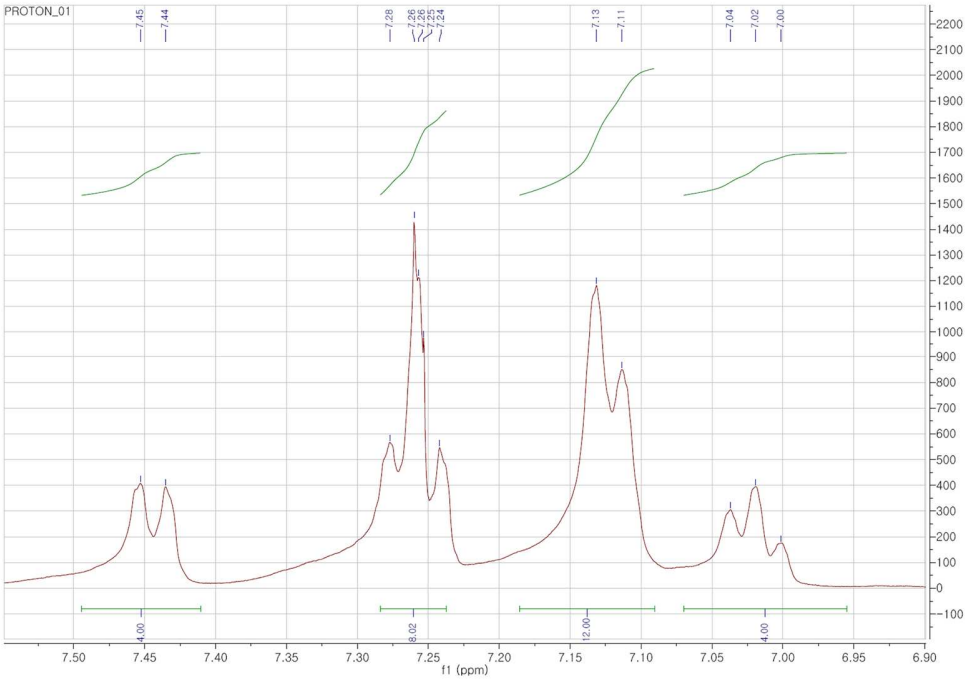

Figure S42. Enlarged ^{1}H-NMR spectrum of M-TPA.

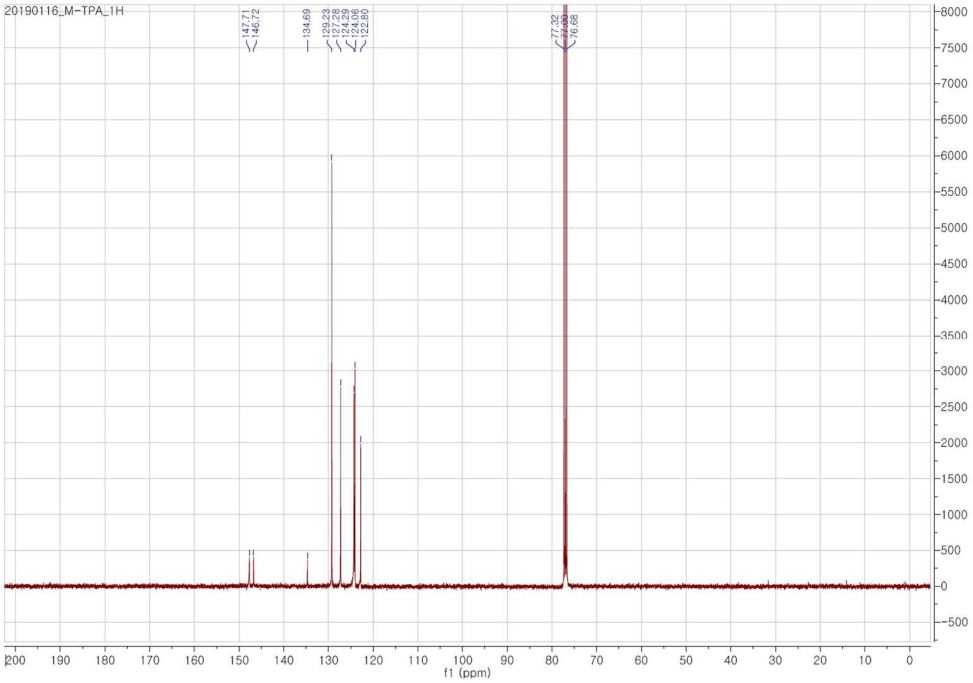

Figure S43. ^{13}C-NMR spectrum of M-TPA.

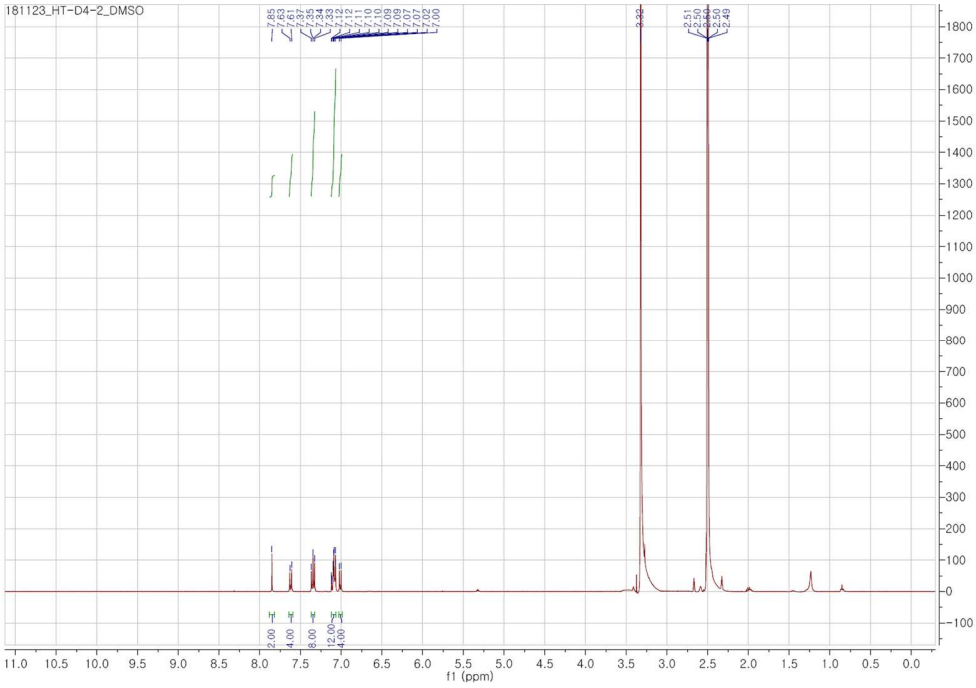

Figure S44. ^{1}H-NMR spectrum of M-DTT.

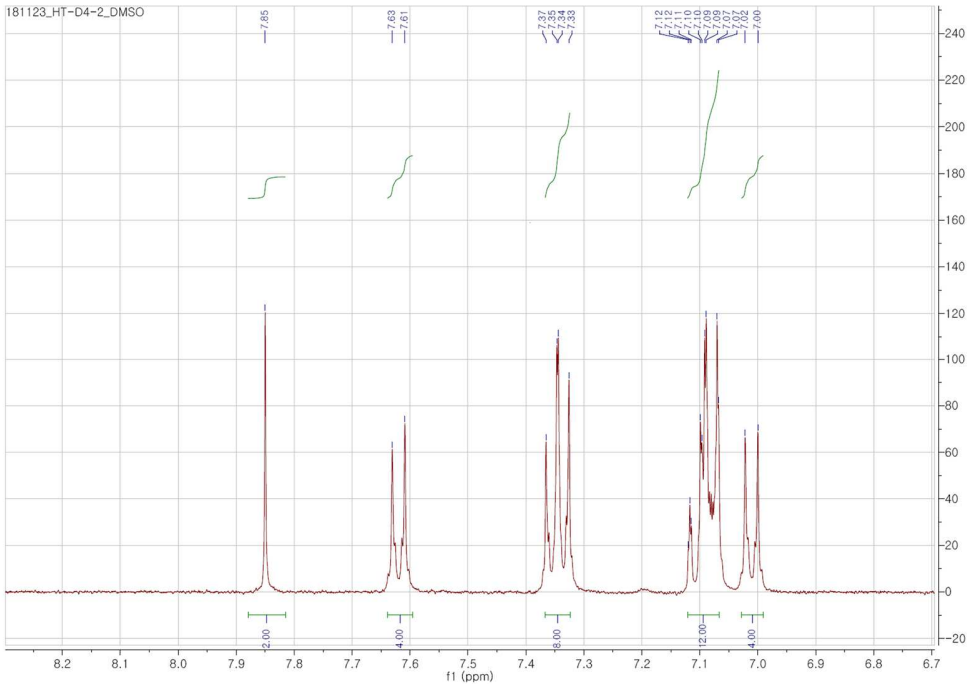

Figure S45. Enlarge ^{1}H-NMR spectrum of M-DTT.

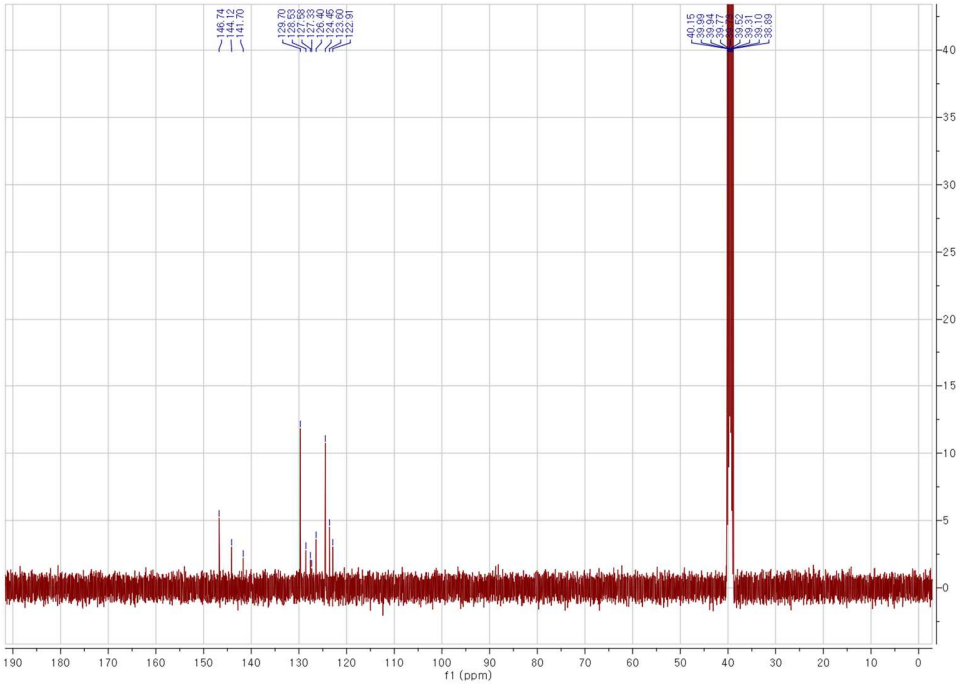

Figure S46. ^{13}C-NMR spectrum of M-DTT.

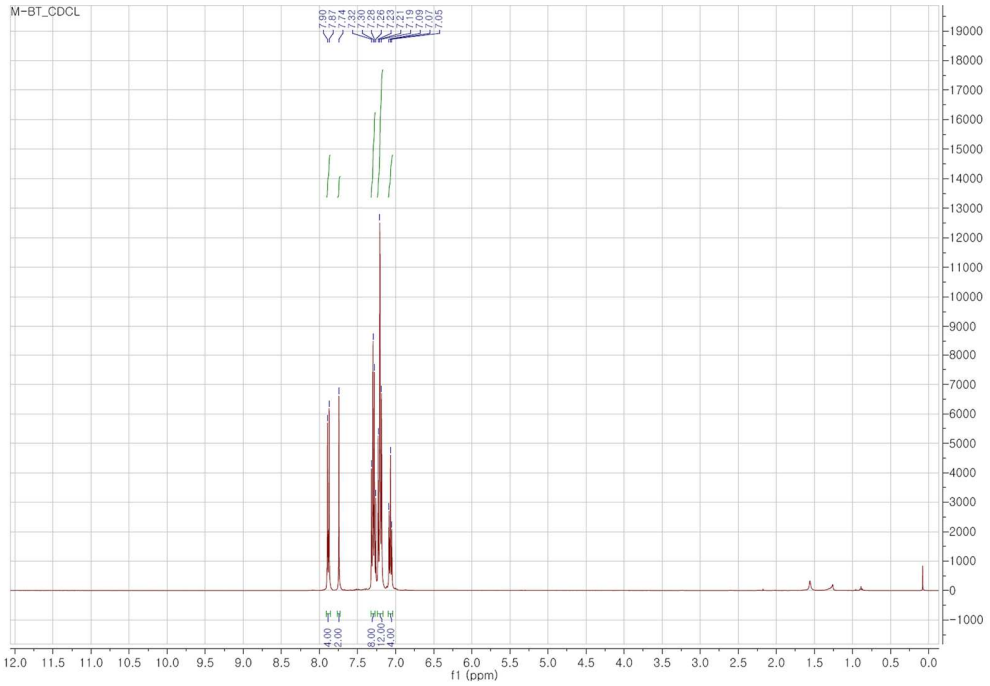

Figure S47. ^{1}H-NMR spectrum of M-BT.

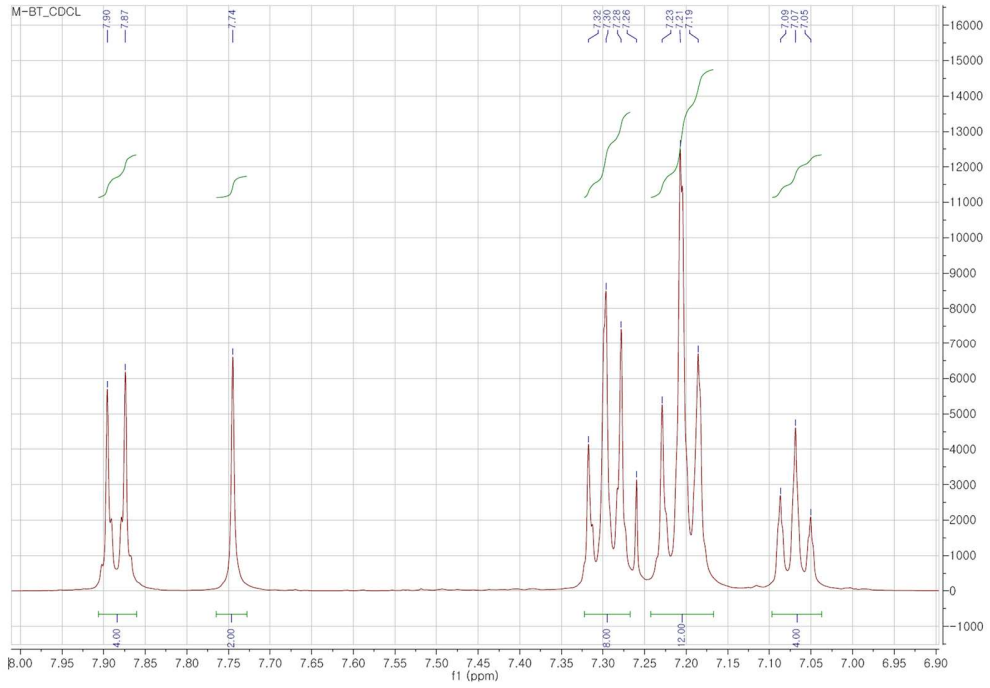

Figure S48. Enlarged ^{1}H-NMR spectrum of M-BT.

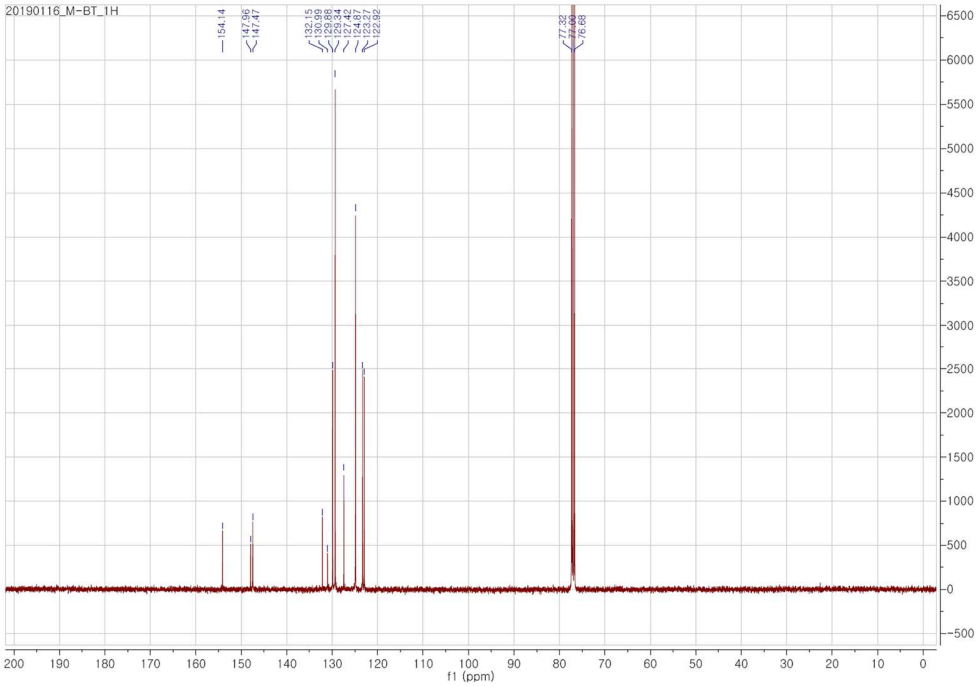

Figure S49. ^{13}C-NMR spectrum of M-BT.

24. References

(1) Yuan, W. Z.; Lu, P.; Chen, S.; Lam, J. W. Y.; Wang, Z.; Liu, Y.; Kwok, H. S.; Ma, Y.; Tang, B. Z. Changing the Behavior of Chromophores from Aggregation-Caused Quenching to Aggregation-Induced Emission: Development of Highly Efficient Light Emitters in the Solid State. *Adv. Mater.* **2010,** *22*, 2159–2163.

(2) Holzer, B.; Bintinger, J.; Lumpi, D.; Choi, C.; Kim, Y.; Stöger, B.; Hametner, C.; Marchetti-Deschmann, M.; Plasser, F.; Horkel, E.; Kymissis, I.; Fröhlich, J. Color Fine-Tuning of Optical Materials Through Rational Design. *ChemPhysChem* **2017,** *18*, 549–563.

(3) Liu, S.; Zhang, H.; Li, Y.; Liu, J.; Du, L.; Chen, M.; Kwok, R. T. K.; Lam, J. W. Y.; Phillips, D. L.; Tang, B. Z. Strategies to Enhance the Photosensitization: Polymerization and the Donor–Acceptor Even–Odd Effect. *Angew. Chem. Int. Ed.* **2018,** *57*, 15189–15193.

(4) Lang, R. J. Ultrasonic Atomization of Liquids. *J. Acoust. Soc. Am.* **1962,** *34*, 6–8.

(5) Nelson, R. R.; Adams, R. N. Anodic Oxidation Pathways of Substituted Triphenylamines. II. Quantitative Studies of Benzidine Formation. *J. Am. Chem. Soc.* **1968,** *90*, 3925–3930.

(6) Lin, H.-Y.; Liou, G.-S. Poly(triphenylamine)s Derived from Oxidative Coupling Reaction: Substituent Effects on the Polymerization, Electrochemical, and Electro-Optical Properties. *J. Polym. Sci., Part A: Polym. Chem.* **2009,** *47*, 285–294.

(7) Thangthong, A. M.; Prachumrak, N.; Tarsang, R.; Keawin, T.; Jungsuttiwong, S.; Sudyoadsuk, T.; Promarak, V. Blue Light-Emitting and Hole-Transporting Materials Based on 9,9-Bis(4-diphenylaminophenyl)fluorenes for Efficient Electroluminescent Devices. *J. Mater. Chem.* **2012,** *22*, 6869–6877.

(8) Gonzalo, S.; Shun, Y. Grazing Incidence Small Angle X-Ray Scattering as a Tool for In-Situ Time-Resolved Studies. In *X-ray Scattering*; IntechOpen, 2017; pp. 29–60.

(9) Smilgies, D.-M. Scherrer Grain-Size Analysis Adapted to Grazing-Incidence Scattering with Area Detectors. *J. Appl. Crystallogr.* **2009,** *42*, 1030–1034.

(10) Chen, W.; Nikiforov, M. P.; Darling, S. B. Morphology Characterization in Organic and Hybrid Solar Cells. *Energy Environ. Sci.* **2012,** *5*, 8045–8074.

(11) Chen, W.; Xu, T.; He, F.; Wang, W.; Wang, C.; Strzalka, J.; Liu, Y.; Wen, J.; Miller, D. J.; Chen, J.; Hong, K.; Yu, L.; Darling, S. B. Hierarchical Nanomorphologies Promote Exciton Dissociation in Polymer/Fullerene Bulk Heterojunction Solar Cells. *Nano Lett.* **2011,** *11*, 3707–3713.

(12) Katsoulidis, A. P.; Dyar, S. M.; Carmieli, R.; Malliakas, C. D.; Wasielewski, M. R.; Kanatzidis, M. G. Copolymerization of Terephthalaldehyde with Pyrrole, Indole and Carbazole Gives Microporous POFs Functionalized with Unpaired Electrons. *J. Mater. Chem. A* **2013,** *1*, 10465–10473.

(13) Xu, C.; Hedin, N. Synthesis of Microporous Organic Polymers with High CO2-Over-N2 Selectivity and CO2 Adsorption. *J. Mater. Chem. A* **2013,** *1*, 3406–3414.

(14) Sreenath, K.; Suneesh, C. V.; Ratheesh Kumar, V. K.; Gopidas, K. R. Cu(II)-Mediated Generation of Triarylamine Radical Cations and Their Dimerization. An Easy Route to Tetraarylbenzidines. *J. Org. Chem.* **2008,** *73*, 3245–3251.

(15) Oyama, M.; Higuchi, T.; Okazaki, S. An Intermediate State of the Triphenylamine Cation Radical Revealed Using an Electron-Transfer Stopped-Flow Method. *Electrochem. Solid-State Lett.* **2002,** *5*, E1–E3.

(16) Pavlishchuk, V. V.; Addison, A. W. Conversion Constants for Redox Potentials Measured Versus Different Reference Electrodes in Acetonitrile Solutions at 25°C. *Inorg. Chim. Acta* **2000,** *298*, 97–102.

(17) Kim, H.-T.; Shin, H.; Jeon, I.-Y.; Yousaf, M.; Baik, J.; Cheong, H.-W.; Park, N.; Baek, J.-B.; Kwon, T.-H. Carbon–Heteroatom Bond Formation by an Ultrasonic Chemical Reaction for Energy Storage Systems. *Adv. Mater.* **2017,** *29*, 1702747.

(18) Chaudhary, M.; Nayak, A. K.; Muhammad, R.; Pradhan, D.; Mohanty, P. Nitrogen-Enriched Nanoporous Polytriazine for High-Performance Supercapacitor Application. *ACS Sustainable Chem. Eng.* **2018,** *6*, 5895–5902.

(19) Yang, Y.; Zhang, P.; Hao, L.; Cheng, P.; Chen, Y.; Zhang, Z. Grotthuss Proton-Conductive Covalent Organic Frameworks for Efficient Proton Pseudocapacitors. *Angew. Chem. Int. Ed*. **2021**, *60*, 21838–21845.

(20) Liao, Y.; Wang, H.; Zhu, M.; Thomas, A. Efficient Supercapacitor Energy Storage Using Conjugated Microporous Polymer Networks Synthesized from Buchwald–Hartwig coupling. *Adv. Mater.* **2018,** *30*, 1705710.

(21) Zhao, Y.; Wang, X.; Xin, T.; Wang, N.; Liu, J. Aqueous Asymmetric Supercapacitors Based on Electrodeposited Poly(1,5-naphthalenediamine) and Poly(4,4´-oxydianiline). *Sustainable Energy Fuels* **2019,** *3*, 3603–3610.

(22) Wang, K.; Huang, L.; Eedugurala, N.; Zhang, S.; Sabuj, M. A.; Rai, N.; Gu, X.; Azoulay, J. D.; Ng, T. N. Wide Potential Window Supercapacitors Using Open-Shell Donor–Acceptor Conjugated Polymers with Stable N-Doped States. *Adv. Energy Mater.* **2019,** *9*, 1902806.

(23) Li, L.; Lu, F.; Xue, R.; Ma, B.; Li, Q.; Wu, N.; Liu, H.; Yao, W.; Guo, H.; Yang, W. Ultrastable Triazine-Based Covalent Organic Framework with an Interlayer Hydrogen Bonding for Supercapacitor Applications. *ACS Appl. Mater. Interfaces* **2019,** *11*, 26355–26363.

(24) Hao, L.; Ning, J.; Luo, B.; Wang, B.; Zhang, Y.; Tang, Z.; Yang, J.; Thomas, A.; Zhi, L. Structural Evolution of 2D Microporous Covalent Triazine-Based Framework Toward the Study of High-Performance Supercapacitors. *J. Am. Chem. Soc.* **2015,** *137*, 219–225.

(25) Zhao, Y.; Liu, J.; Wang, N.; Li, Q.; Hu, M. Rational Selection of Small Aromatic Molecules to Functionalize Graphene for Enhancing Capacitive Energy Storage. *J. Mater. Chem. A* **2018,** *6*, 7566–7572.

(26) Chandra, S.; Roy Chowdhury, D.; Addicoat, M.; Heine, T.; Paul, A.; Banerjee, R. Molecular Level Control of the Capacitance of Two-Dimensional Covalent Organic Frameworks: Role of Hydrogen Bonding in Energy Storage Materials. *Chem. Mater.* **2017,** *29*, 2074–2080.

(27) Khattak, A. M.; Ghazi, Z. A.; Liang, B.; Khan, N. A.; Iqbal, A.; Li, L.; Tang, Z. A Redox-Active 2D Covalent Organic Framework with Pyridine Moieties Capable of Faradaic Energy Storage. *J. Mater. Chem. A* **2016,** *4*, 16312–16317.